Large-Scale Structure in Wind Forcing over the California Current System in Summer

MELANIE R. FEWINGS

Department of Marine Sciences, University of Connecticut, Groton, Connecticut

(Manuscript received 19 April 2017, in final form 8 July 2017)

ABSTRACT

The wind that drives oceanic eastern boundary upwelling systems is highly variable. In many locations, the standard deviation of wind velocity on time scales of days to weeks is larger than the mean. In the ~1600-km-long California Current System (CCS), the spatial decorrelation scale of the wind fluctuations is ~400–800 km, suggesting wind fluctuations in the north and south ends of the system are not related. Yet, there is also the suggestion in the literature of a larger-scale structure in the fluctuations. Here, empirical orthogonal function (EOF) analysis of buoy and satellite wind velocities confirms the existence of that structure. This analysis covers a larger spatial domain than previous EOF studies in the CCS and, to allow for propagation of the wind fluctuations, includes an approach for calculating Hilbert EOFs from time series with gaps. The large-scale structure in the wind fluctuations is a quasi-dipole pattern spanning the coastline from Washington through California. It accounts for ~60% of the wind velocity variance on time scales of days to weeks. The time-mean wind velocity, showing a continuous zone of intensified wind along the coast, is deceptive. When the northern half of the CCS is in a relaxation state, the southern half often experiences intensified winds, and vice versa. There should be a resulting out-of-phase structure in oceanic upwelling. The out-of-phase wind fluctuations in the north and south parts of the CCS may affect the forcing of oceanic coastal-trapped waves, mesoscale eddy generation at capes, and offshore export of carbon.

1. Introduction

Wind-driven coastal upwelling in eastern boundary upwelling systems such as the California Current System (CCS; e.g., Huyer 1983) supplies nutrients that fuel phytoplankton growth and support high fisheries productivity (e.g., Pauly and Christensen 1995). Although the prevailing wind is upwelling favorable in the CCS and other eastern boundary upwelling systems, the wind field can be highly variable. In the CCS, the wind velocity fluctuations are comparable to the mean or larger (Halliwell and Allen 1987) (Fig. 1). The wind fluctuates because of synoptic-scale pressure changes associated with movement of the jet stream and offshore anticyclone, in the case of the CCS the North Pacific high (NPH), and its interaction with the low-pressure area over the desert in the southwestern United States (Mass and Bond 1996; Bane et al. 2005; Nuss 2007). Within a few tens of kilometers of the coast, these wind velocity fluctuations can be enhanced by smaller-scale processes involving the marine boundary layer and the coastal mountains [reviewed in Nuss et al. (2000)]. The resulting weak wind events, or "relaxations," and wind reversals reduce offshore Ekman transport in the surface layer and cause temporal variability in oceanic upwelling (e.g., Winant et al. 1987). In all four major eastern boundary upwelling systems, wind relaxations also allow buoyant poleward along-coast flows of warm water that affect coastal water temperatures and can transport larvae (Send et al. 1987; Relvas and Barton 2002, 2005; García-Lafuente et al. 2006; Fawcett et al. 2008; Melton et al. 2009; Washburn et al. 2011; Garel et al. 2016). Therefore, it is important to understand the variability in the wind field over eastern boundary upwelling systems.

In the CCS, the spatial correlation scale of the wind variability is thought to be smaller than the scale of the upwelling system, which is ~1600 km. The decorrelation scale of the wind field is 400–800 km in summer, and the along-coast correlation of wind velocity is weak across Cape Mendocino, near the center of the system (Halliwell and Allen 1987). Previous empirical orthogonal function (EOF) analyses of the wind field in summer focused on subdomains of the CCS. For the southern and central

Corresponding author: Melanie R. Fewings, melanie.fewings@uconn.edu

DOI: 10.1175/MWR-D-17-0106.1

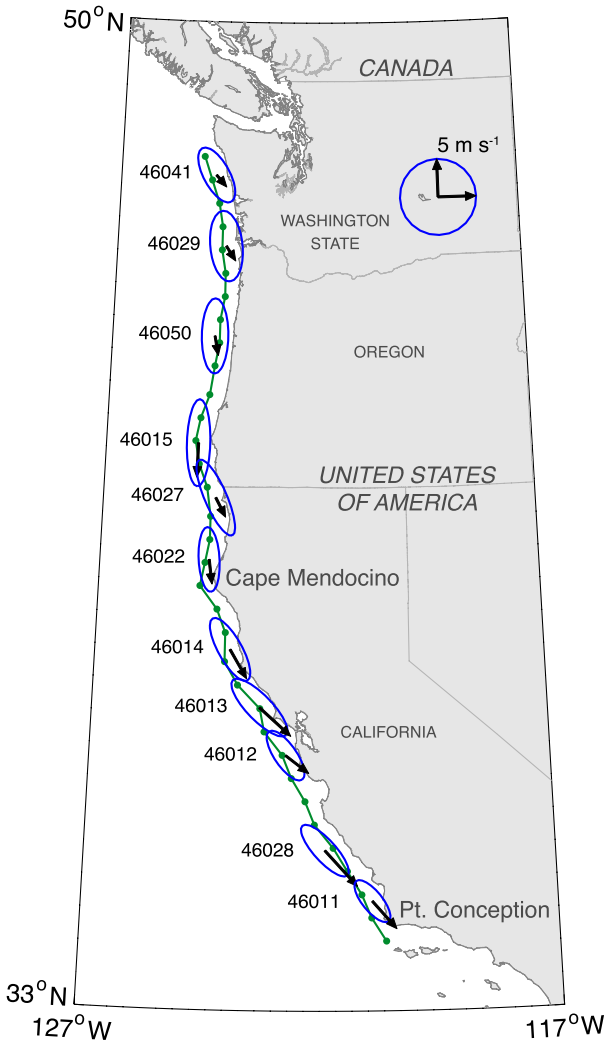

FIG. 1. Mean wind velocity and its variability over the CCS in summer, from NDBC buoys during June–September 1981–2016. Black vectors show the mean wind velocity; the buoys are located at the tails of the vectors. Blue principal axis ellipses indicate the standard deviation of wind velocity on time scales of days and longer. Buoy numbers are given at left. Green connected dots following the coast indicate the locations of QuikSCAT satellite vector wind data used in other figures.

CCS, the leading mode has large amplitude over only a portion of the analysis domain (Kelly 1985). For the central and northern CCS, modes with large amplitude south of Cape Mendocino have small amplitude north of Cape Mendocino, suggesting the wind variability in the poleward and equatorward parts of the system is in independent modes (Perlin et al. 2004). As a result, there is a conception in the literature that wind relaxation or reversal events in the poleward and equatorward parts of the CCS, north and south of Cape Mendocino, are not connected.

However, the literature also suggests a larger-scale structure is present in the wind field. Halliwell and Allen (1987) described "event sequences" of alternating wind reversal and intensification that affect the poleward part of the CCS, from Washington to Cape Mendocino. These event sequences are driven by synoptic-scale pressure fluctuations associated with troughs or extratropical cyclones propagating on the jet stream (Bane et al. 2005), followed by NPH extension and ridging over the CCS (e.g., Taylor et al. 2008). However, if NPH ridging is strong enough it leads to wind reversal in the equatorward part of the CCS, from Point Conception to Cape Mendocino and occasionally farther, by advecting the desert heat low offshore and weakening the along- and cross-coast atmospheric pressure gradients (Mass and Bond 1996; Nuss 2007). The connection of wind reversals in both the equatorward and poleward parts of the CCS to similar NPH ridging events suggests winds along the entire CCS may be related in a coherent fashion.

Recent work supports this idea of system-wide coherence in the wind field. In a composite of summer wind relaxations off central California, the winds off Oregon tend to relax or reverse ~5 days previous to and ~5 days after the central California relaxation (Fewings et al. 2016). The wind relaxations off central California are caused by a weaker version of the same NPH ridging that causes the wind reversals discussed by Mass and Bond (1996) and Nuss (2007). This indicates the event sequence described by Halliwell and Allen (1987) has three, not two, stages: wind relaxation or reversal in the poleward part of the CCS; followed by wind intensification; followed by wind relaxation, or more rarely reversal, in the equatorward part of the CCS. The entire sequence takes ~10–12 days on average (Fewings et al. 2016). The wind relaxations that occur poleward and equatorward of Cape Mendocino are caused by different mechanisms but are connected by an NPH ridging event that reintensifies the wind and separates the two relaxations in time. Because of this three-stage wind event sequence, we would therefore expect coherent time variability in the wind field along the entire coast. In fact, there is already the suggestion of correlation in the wind field on scales larger than 800 km in Halliwell and Allen (1987, their Fig. 6). Although the correlation between winds at buoy pairs drops to zero near Cape Mendocino, winds off central California are somewhat *negatively* correlated with winds off Oregon and Washington (Fig. 2). This tantalizing evidence of a large-scale structure that unifies the wind variability along the entire CCS was the motivation for the present study.

Here, the temporal variation in the along-coast wind velocity from Washington to California is analyzed using EOFs and Hilbert EOFs of buoy and satellite data. This analysis includes an approach for calculating Hilbert EOFs from time series with gaps, described in section 2.

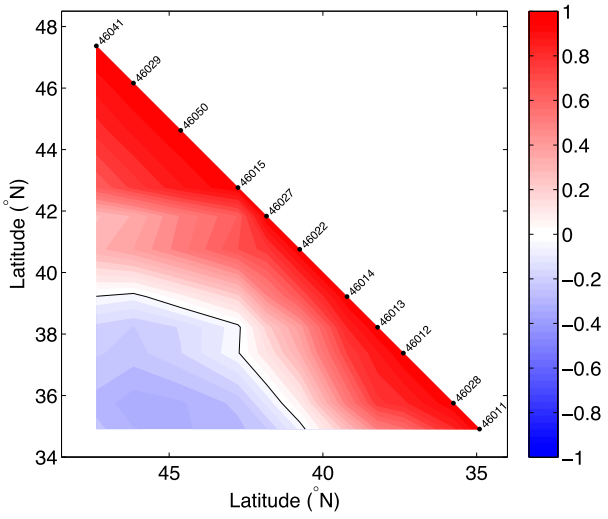

FIG. 2. Contours of the correlation matrix (r) at zero time lag between along-coast wind velocities at pairs of buoys along the coast during June–September 1981–2016. Similar to Halliwell and Allen (1987, their Fig. 6). Data overlap varies depending on the buoy pair. Buoy numbers are indicated along the diagonal. See Fig. 1 for buoy locations. The wind velocities were low-pass filtered with a $(48\,\mathrm{h})^{-1}$ cutoff to remove the diurnal cycle. An independence time scale of 2.5 days is used, based on the autodecorrelation time scales of ~2.5–3 days for individual buoys. The minimum r for 95% significance is 0.06–0.1 depending on the buoy pair. The zero contour is shown in black.

There is system-wide structure in the wind field, presented in sections 3 and 4. A single coast-wide Hilbert EOF mode explains much of the wind velocity variance in summer. Section 5 discusses how in correlation analysis between buoy pairs the relation between winds in the northern and southern parts of the system does not appear as strong, likely due to frontal systems. Section 6 shows how the large-scale structure can be interpreted in light of the three-stage wind cycle discussed above, as well as implications for the structure of coastal upwelling and generation of mesoscale eddies.

2. Data and methods

a. *Buoy wind data*

Hourly wind velocities from 11 National Data Buoy Center (NDBC) buoys during June–September 1981–2016 (Figs. 1, 3) are included in the analysis. Gaps <12 h long were filled by linear interpolation. The data were then low-pass filtered with a $(48\,\mathrm{h})^{-1}$ half-amplitude cutoff to remove the diurnal cycle, which constitutes ~10% of the wind velocity variance and is not the focus of this study. Below, "total variance" refers to total variance on time scales >48 h. The spatial patterns presented below are not sensitive to applying this low-pass filter, removing an annual climatology, or including May or leaving out September.

b. *Satellite ocean vector wind data*

The satellite data are QuikSCAT Level 2B version 3.1 swath data (SeaPAC 2016), which are provided at http://podaac.jpl.nasa.gov on a 12.5-km grid. These are equivalent 10-m neutral winds derived from microwave backscatter from ocean surface roughness (Fore et al. 2014). The data are available during 27 October 1999 to 22 November 2009 (Fig. 3). The QuikSCAT wind velocities from each swath were linearly interpolated onto a 0.1° latitude–longitude grid by Delaunay triangulation. These winds were then rotated into the along-coast coordinate system described below. Short gaps, mostly ≤24 h, at some coastline locations due to

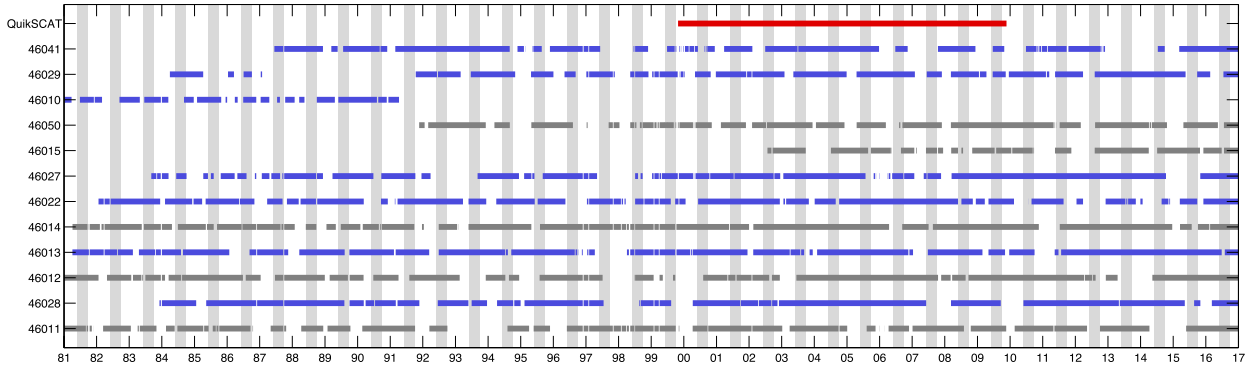

FIG. 3. Timeline of data availability for QuikSCAT and the NDBC buoys during 1981–2016. The last two digits of the year are indicated along the lower axis. Horizontal bars indicate periods when wind velocity data are available. Buoy numbers are indicated at left. Buoy time series shown in blue were used in the HEOF analysis. Buoy time series shown in blue and dark gray were included in the standard EOF analysis, except buoy 46010, which was used only in the HEOF analysis for the Mass and Bond (1996) time period because of a lack of data availability after 1991. Data availability for all months of the year is shown here for context, though only June–September buoy data were used in this study (indicated by vertical gray shading).

satellite approach angle were filled by interpolating the available data onto an hourly time base using Delaunay triangulation as a function of latitude and time, then low-pass filtering similarly to the buoy data above, then subsampling onto a 12-h time base. As for the buoy data, in the text below, "total variance" refers to total variance on time scales >48 h. The results below are not sensitive to the specifics of the interpolation procedure. A time series of the gridded satellite winds was extracted every 0.4° latitude on a line following the coast (Fig. 1). The results are similar if the line is moved 10–30 km offshore, or if QuikSCAT Level 2B version 3.0 data are used instead, though those data are not available as close to the coast as version 3.1.

c. Coordinate system

The along-coast coordinate system at each buoy or satellite vector wind grid point is based on coastline direction. High-resolution coastline data from the NOAA Global Self-Consistent Hierarchical High-Resolution Shorelines database were adjusted to remove large bays such as San Francisco Bay and then low-pass-filtered as a function of along-coast distance with a $(150\,\mathrm{km})^{-1}$ half-amplitude cutoff. The large-scale modal structures presented below still exist if the north–south component of wind velocity, or principal axis coordinates, are used instead of this along-coast coordinate system. Principal axis coordinates are not ideal near capes, however, where the principal axis of variability is different for upwelling- versus downwelling-favorable winds due to the sharp change in coastline angle.

d. Standard EOF calculations

The EOFs of the along-coast component of the wind velocity, hereafter called "standard EOFs" to distinguish from Hilbert EOFs, were calculated from the 377 days during June–September 1981–2016 with data available simultaneously at all 11 buoys, which occurred during 2002–04, 2006, 2008–11, and 2016. First, the mean was removed from each time series. Each time series was then standardized by dividing by its standard deviation. The EOFs were calculated from the covariance matrix of the scaled time series. The scaling by standard deviation makes the standard EOF calculation consistent with the Hilbert EOF (HEOF) calculation described below and is equivalent to using the correlation matrix to find the EOFs (e.g., Wallace and Dickinson 1972; Björnsson and Venegas 1997). Without this standardization, the results are not qualitatively different; the spatial amplitude pattern is more variable across the domain, but not markedly so (not shown), because the wind variability has a fairly similar magnitude at all sites (Fig. 1). The time series of the standard EOF modes were also scaled to have standard deviation = 1, and the spatial patterns of the EOF modes scaled to compensate, so that all velocity scale factors are in the spatial parts of the modes.

e. The HEOF technique

HEOF analysis is a statistical technique that, unlike standard EOF analysis, can capture a propagating pattern in a single mode (e.g., Hannachi et al. 2007). HEOFs are calculated as complex-valued EOFs calculated from the covariance matrices of the Hilbert-transformed time series (e.g., Horel 1984; Merrifield and Guza 1990; Björnsson and Venegas 1997; Hannachi et al. 2007). Here, the technique is reviewed following those references.

Similarly to standard EOF analysis, Hilbert EOF analysis begins with a group of real-valued time series of data from various locations. First, the time mean should be removed at each location, and the resulting time series should be tapered to avoid end effects (see section 2f). The resulting demeaned, tapered time series at the jth site is $u_j(t)$. Using Fourier analysis, $u_j(t)$ can be expressed as a sum of sines and cosines:

$$u_j(t) \equiv \sum_{\omega} [a_j(\omega)\cos(\omega t) + b_j(\omega)\sin(\omega t)], \qquad (1)$$

where ω is angular frequency and $a_j(\omega)$ and $b_j(\omega)$ are the Fourier coefficients of $u_j(t)$. Using these coefficients, one can define the quadrature function of $u_j(t)$, called $\hat{u}_j(t)$:

$$\hat{u}_j(t) \equiv \sum_{\omega} [a_j(\omega)\sin(\omega t) - b_j(\omega)\cos(\omega t)], \qquad (2)$$

so that $\hat{u}_j(t)$ is the same as the original time series, except each spectral component has a phase shift of $\pi/2$. This function $\hat{u}_j(t)$ is the Hilbert transform of $u_j(t)$.

Next, an auxiliary time series $U_j(t)$ is constructed from the original time series $u_j(t)$ and its Hilbert transform $\hat{u}_j(t)$:

$$U_j(t) \equiv u_j(t) + i\hat{u}_j(t). \qquad (3)$$

[Here, this was done using the MATLAB function "hilbert," which directly returns $U_j(t)$, not $\hat{u}_j(t)$.] The time series $U_j(t)$ for all sites j, where $j = 1, \ldots, M$, are then collected as the columns of a matrix $\mathbf{U}$ in which each column is a location and each row is a sampling time. This matrix is then analyzed similarly to standard EOF methods. First, one calculates the complex covariance matrix of $\mathbf{U}$:

$$\mathbf{F} = \frac{1}{N-1}\mathbf{U}^{\dagger}\mathbf{U}, \qquad (4)$$

where N is the number of samples in time and † indicates the conjugate transpose. The eigenfunctions of $\mathbf{F}$ are c_m,

the $m = 1, \ldots, M$ spatial patterns of the HEOF modes. Because **U** and **F** are complex, the spatial pattern of each HEOF mode is complex, unlike in standard EOF analysis. We can write each complex spatial pattern c_m in terms of a real-valued spatial amplitude γ_m and a real-valued spatial phase θ_{sm}:

$$c_m \equiv \gamma_m e^{i\theta_{sm}}, \tag{5}$$

where

$$\gamma_m = |c_m|, \tag{6}$$

and

$$\theta_{sm} = \tan^{-1}\left[\frac{\mathrm{Im}(c_m)}{\mathrm{Re}(c_m)}\right]. \tag{7}$$

The spatial phase indicates the phase lag of the fluctuations at each site with respect to a reference site. [Note that in Merrifield and Guza (1990) and Hannachi et al. (2007) there is a minus sign in their version of Eq. (7), which compensates for a minus sign in their definition of the Hilbert transform.]

The eigenvalues of **F** are λ_m. The percent of the total variance of the original M time series from all sites that is captured by the mth mode, P_m, is determined from the eigenvalues as

$$P_m = 100\% \times \left(\frac{\lambda_m}{\sum_{m=1}^{M}\lambda_m}\right). \tag{8}$$

A 95% confidence interval for P_m is (North et al. 1982):

$$P_{95\%m} = \left(1 \pm \sqrt{\frac{2}{N}}\right)P_m. \tag{9}$$

If the N data points in each time series are not independent, N in Eq. (9) should be replaced with an estimate of the number of independent points. Here, the independence time is assumed to be 10 days, based on the three-stage wind event sequence time scale (section 6a). Note that for standard EOFs of complex time series, the factor of 2 under the square root in Eq. (9) is removed because the real and imaginary parts of the complex time series are assumed to be independent, so the time series has $2N$ degrees of freedom. That is not the case here because, although $U_j(t)$ is complex, the imaginary part is constructed from the real part, and the Hilbert transform does not add any new degrees of freedom to $U_j(t)$.

The time series of the mth mode $a_m(t)$ is found the same way as in standard EOF analysis, by projecting the spatial pattern of the mth mode onto the matrix **U** of data time series from all sites:

$$a_m(t) = \mathbf{U}c_m. \tag{10}$$

These modal time series are also complex. A real-valued temporal amplitude a_{0m} and real-valued temporal phase θ_{tm} can be defined similarly to Eqs. (5)–(7):

$$a_m(t) = \alpha_m(t)e^{i\theta_{tm}(t)}, \tag{11}$$

where

$$\alpha_m = |a_m| \tag{12}$$

and

$$\theta_{sm} = \tan^{-1}\left[\frac{\mathrm{Im}(c_m)}{\mathrm{Re}(c_m)}\right]. \tag{13}$$

The percent of the variance at site j that is captured by the mth mode is equal to the correlation coefficient squared between the time series from the jth site $U_j(t)$ and the time series of the mth mode $a_m(t)$. A more computationally efficient way to calculate this quantity is

$$\text{percent variance captured at } j\text{th site by } m\text{th mode} = 100\% \times \left(c_{jm}c_{jm}^{*}\frac{\lambda_m}{\sigma^2_{U_j(t)}}\right), \tag{14}$$

where the asterisk (*) indicates the complex conjugate and $\sigma^2_{U_j(t)}$ is the variance of the time series $U_j(t)$.

The time series $U_j(t)$ can be reconstructed for any site j by summing over all the modes:

$$U_j(t) = \sum_{m=1}^{M} a_m(t)c_{mj}^{\dagger}, \tag{15}$$

and the original scaled time series $u_j(t)$ can be found from $u_j(t) = \mathrm{Re}[U_j(t)]$. When plotting a single HEOF mode m at a particular site j, typically only the real part of the HEOF is plotted, for example, $\mathrm{Re}[a_m(t)c_{mj}^{\dagger}]$, because, similarly to $U_j(t)$, the imaginary part of each HEOF mode is the Hilbert transform of the real part, that is, the same as the real part but with a phase shift of $\pi/2$.

For more details on EOFs and HEOFs, see Wallace and Dickinson (1972), Horel (1984), Merrifield and Guza (1990), Björnsson and Venegas (1997), and Hannachi et al. (2007).

f. HEOF calculations from the continuous QuikSCAT time series

The Hilbert transform is typically calculated from the Fourier coefficients of a time series, which requires gap-free time series. Therefore, it is straightforward to calculate HEOFs from the continuous 1999–2009 QuikSCAT time series of along-coast wind velocity, which includes all seasons. First, the time mean was removed at each site. Then a cosine, or Tukey, taper was applied to the first and last 5% of the time series. Each time series was then standardized by multiplying by $1/\sigma$ where σ is the standard deviation of the time series, to be consistent with the standardization in section 2d. Next, the entire 1999–2009 time series of wind velocity at each location, including all months of the year, was Hilbert transformed (section 2e). Finally, the complex EOFs were calculated by taking only the June–September time periods of the Hilbert-transformed 1999–2009 time series, joining those chunks end-to-end, then calculating the covariance matrix and its complex EOFs, the HEOFs. Similarly to the EOFs in section 2d, the time series of the resulting HEOFs were scaled to have standard deviation = 1 by multiplying each modal time series $a_m(t)$ by $1/\sigma_m^a$, where σ_m^a is the standard deviation of $\mathrm{Re}[a_m(t)]$, and the spatial patterns scaled to compensate by multiplying by σ_m^a. The spatial phase patterns θ_{sm} (section 2e) are arbitrary to within a constant offset, which can be absorbed into the temporal phase θ_{tm} at each site (e.g., Merrifield and Guza 1990; Hannachi et al. 2007); here, the spatial phase is set to zero at the southernmost location. The results of this procedure are referred to in section 4 as "QuikSCAT 1 Hilbert" because the entire QuikSCAT time series is Hilbert transformed as one continuous segment.

g. HEOFs from data with gaps

Calculating the HEOFs from the buoy data is more complicated because of the gaps in the time series. However, only the Hilbert transform operation requires continuous time series. The covariance and the complex EOF calculations do not. Therefore, the HEOFs can be calculated by carrying out the Hilbert transform on each available segment of data separately, joining the Hilbert-transformed time series end-to-end, and then calculating the complex HEOFs. This procedure was tested with the QuikSCAT data. The time mean was removed from each June–September time series segment available during 2000–09. A cosine taper was applied to the first and last 5% of each segment. Each segment was standardized as in section 2f but using the standard deviation of the concatenated segments. These demeaned, tapered, standardized QuikSCAT time series segments were each Hilbert transformed separately. The Hilbert-transformed segments were then appended end-to-end. The covariance matrix was calculated from this concatenated time series, and the HEOFs were calculated from the covariance matrix as in section 2f.

The results of calculating the HEOFs from the discrete June–September chunks of QuikSCAT data are very similar to the results of calculating the HEOFs by Hilbert transforming the entire QuikSCAT time series at once (section 2f), as will be shown in section 4. The results are not identical because the continuous year-round 1999–2009 time series resolves lower-frequency variations than the individual June–September chunks. If a high-pass filter with a $(120\ \mathrm{day})^{-1}$ half-amplitude cutoff, where the cutoff is based on the ~120 days in June–September, is applied to the 1999–2009 QuikSCAT time series before calculating the Hilbert transform in section 2f, the results become nearly identical (not shown); the very small remaining discrepancy may be because the filter does not have a sharp cutoff. This gives confidence in calculating HEOFs from the buoy data, where it would not be possible to Hilbert transform the entire time series simultaneously without interpolating across large gaps (Fig. 3).

To resolve synoptic time scales with statistical confidence, only time periods when all buoys had data for at least 20 days continuously were included in the buoy HEOF calculations. This is unlike the standard EOF calculations in section 2d, where shorter time periods of data were also included. [Although reanalysis winds are a continuous alternative to buoy data, reanalysis winds are not used here because they do not resolve well the wind maxima along the coast caused by the five major capes (e.g., Perlin et al. 2004; Fewings et al. 2016).] The buoy HEOFs were calculated similarly to the HEOFs of the discrete June–September QuikSCAT chunks in the above paragraph. Segments of continuous data longer than 20 days are available simultaneously at all 11 buoys during summer 2003, 2004, 2009, 2011, and 2016, for a total of 270 days in the concatenated Hilbert-transformed time series in the buoy HEOF analysis.

To extend the HEOF results farther back in time and enable comparison with the Mass and Bond (1996) and Bond et al. (1996) studies of wind reversals (see section 2j), the HEOFs were also calculated with a subset of six buoys: 46041, 46029, 46027, 46022, 46013, and 46028. For this analysis only, wind velocity from buoy 46029 was combined with the time series from a nearby buoy, 46010, to increase the data coverage during 1981–91 (Fig. 3).

h. Correlation calculations

Pearson linear correlation coefficients were calculated from the filtered buoy wind velocity data at time lags of −20 to 20 days in intervals of 1 h, using all times in June–September 1981–2016 with data available at both buoys in each pair. Unless otherwise noted, all correlations reported here are significant at the 95% confidence level, using an independence time scale of ~2.5–3 days, equal to the decorrelation time scale calculated following Thomson and Emery (2014).

i. Coherence calculations

To determine what percentage of the variability in any two time series is lag correlated, when the time lag is unknown and may differ for different frequency bands, we can examine the magnitude and phase of the coherence spectrum (e.g., Thomson and Emery 2014). A coherence spectrum C_{xy} is a normalized cross spectrum:

$$C_{xy}(f) \equiv \frac{S_{xy}(f)}{\sqrt{S_{xx}(f)S_{yy}(f)}}, \tag{16}$$

where S_{xy} is the cross-spectral density of the two time series $x(t)$ and $y(t)$, f is frequency, and S_{xx} and S_{yy} are the autospectral densities. The magnitude squared of the coherence spectrum, $|C_{xy}|^2$, can have values from 0 to 1, and the coherence phase is $\phi(f)$, calculated from

$$C_{xy}(f) = |C_{xy}(f)|e^{i\phi(f)}. \tag{17}$$

Here, the coherence between the time series of buoy EOFs 1 and 2 was calculated from the gap-free chunks of data that were at least 17 days long, following Aristizábal et al. (2016, 2017).

j. Identifying wind relaxations and reversals

The onset times of wind relaxation events at Point Conception were identified by Melton et al. (2009). The times were defined based on zero crossings of the first EOF of the $(36\,\text{h})^{-1}$ low-pass-filtered, major principal axis wind velocity at NDBC buoys 46062, 46011, 46023, and 46054 near Point Conception. The EOF was required to be mostly negative for the preceding ~2 days and mostly positive for the following ~2 days or more. Since the first EOF captures 80% of the wind velocity variance, the Melton et al. (2009) index essentially identifies times when the wind velocity at Point Conception falls below its mean value for a couple of days or longer. Here, the Melton et al. (2009) method was used to identify wind relaxations over the entire buoy record in Fig. 3.

The times of coastally trapped wind reversals were identified in Mass and Bond (1996) and Bond et al. (1996), using hourly wind data from NDBC buoy 46013 off California and other buoys. They identified times when the wind shifted from northerly to southerly. The wind was required to be northerly for most of the preceding 12 h and southerly for most of the following 12 h. The wind direction after the reversal to southerly was required to be within 45° of the along-coast direction. In the analysis here, the times of strong wind reversals at buoy 46013 listed in Bond et al. (1996) and weak wind reversals at buoy 46013 listed in Mass and Bond (1996) are grouped together.

3. A large-scale dipole structure in the buoy wind field

a. The first EOF of buoy winds: A dipole mode

In summer, the leading standard EOF of along-coast wind velocity at the 11 NDBC buoys is a dipole mode (Fig. 4a). While the wind velocity is from one direction off Washington and Oregon, the wind tends to be from the opposite direction off California. This EOF captures 44% of the total variance. The node of the dipole is near Cape Mendocino, where the amplitude of the EOF is negligible and almost none of the wind velocity variance is explained (Fig. 4a, "node"). Away from the node, this dipole EOF explains 45%–65% of the variance at individual buoys (Fig. 4b). This EOF shows that the primary pattern of summer wind variability near the coast in the CCS is one in which the poleward and equatorward parts of the system experience wind fluctuations of alternating sign on time scales of days and longer.

b. The second and higher EOFs of buoy winds

In contrast to the dipole mode above, the second EOF has the same sign over the entire region (Fig. 5a). EOF 2 explains 33% of the total along-coast wind velocity variance. However, the spatial amplitude of EOF 2 is larger in the middle part of the CCS (Fig. 5a) and the percent variance explained by EOF 2 is also larger at sites in the middle of the system: 35%–70% off Northern California, but ~15% or less off Washington and central California (Fig. 5b).

EOFs 1 and 2 do not have statistically distinct eigenvalues, according to the North et al. (1982) rule. The 95% confidence intervals of the eigenvalues overlap (not shown), assuming the independence time scale is 10 days or longer, based on the three-stage wind event sequence discussed in sections 1 and 6a. This indicates that EOFs 1 and 2 are degenerate and EOF 2 cannot be neglected. In fact, EOFs 1 and 2 are partially related, as discussed in section 3c below.

Together, EOFs 1 and 2 account for ~80% of the total variance in along-coast wind velocity and ~55%–90%

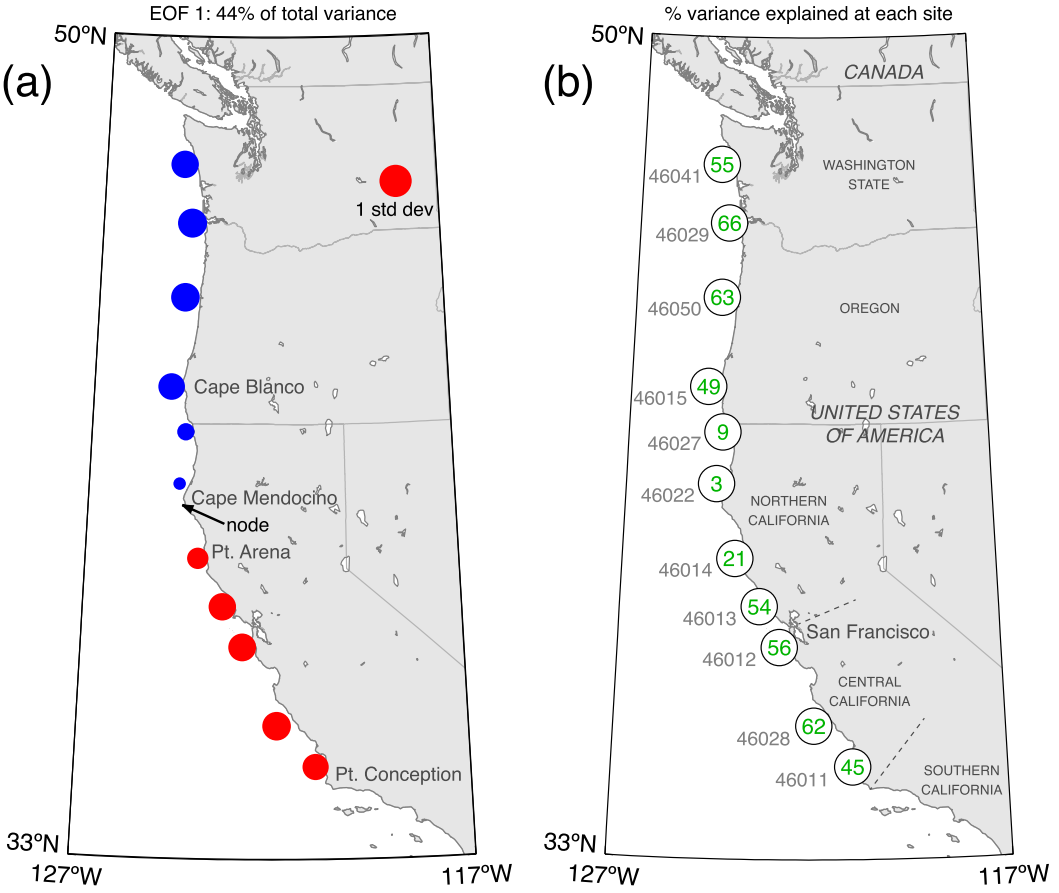

FIG. 4. EOF 1 of the along-coast component of wind velocity at the 11 buoys. (a) Spatial pattern of the EOF. The area of each circle indicates the amplitude of the spatial pattern at that buoy location, in units of the standard deviation of wind velocity at that site (semimajor axis of the ellipse in Fig. 1). Blue and red indicate negative and positive signs, respectively, for the spatial response at each buoy location. (b) Green numbers indicate the percentage of velocity variance captured at each site by this EOF. NDBC buoy number is shown at left of each site.

of the variance at any single buoy (Fig. 6). EOF 3 captures 10% of the overall variance, and EOFs 4–10 each capture <5% of the total wind velocity variance (not shown). Therefore, EOFs 3 and higher are of negligible importance compared to EOFs 1 and 2.

c. *Propagating fluctuations revealed in coherence between buoy EOFs 1 and 2*

Although EOFs 1 and 2 are orthogonal by definition, and their time series are uncorrelated at zero lag, EOFs 1 and 2 are partially related. To understand how EOFs 1 and 2 can be orthogonal and therefore uncorrelated (at zero time lag), yet be related, we can think of the example of two simple time series: $\sin(2\pi ft)$ and $\cos(2\pi ft)$, where the frequency f is constant and t is time. These time series are orthogonal, and they are uncorrelated at zero lag. However, the two time series are clearly related: one is the same as the other, except for a 90° phase lag. The two time series are perfectly correlated at a lag of 90°, equivalent to a time lag of $1/4f^{-1}$. In an analogous manner, the time series of EOFs 1 and 2 are correlated at a lag of several days to weeks, as shown below.

The time series of EOFs 1 and 2 have magnitude squared coherence $|C_{xy}|^2 \sim 0.3$–0.4 at periods of several days to weeks, which is significant at the 95% confidence level (Fig. 7a). The coherence phase is $\phi \sim 90°$ for those periods, indicating EOF 2 is ~90° out of phase with EOF 1 (Fig. 7b). Any two EOFs that are 90° out of phase and 100% coherent can be interpreted as a single, propagating pattern (e.g., Hannachi et al. 2007), similarly to the analogy of a single sine and cosine given above. Here, ~40% of the variance in EOFs 1 and 2 is coherent and 90° out of phase. That indicates that ~40% of the variance in the alternating wind fluctuations is propagating along the coast. This is consistent with previous studies (section 1) and is visually evident in Hovmöller diagrams of EOF 1 (Fig. 8a), EOF 2 (Fig. 8b), and the sum of EOFs 1 and 2 (Fig. 8c) as compared to the measured wind velocity

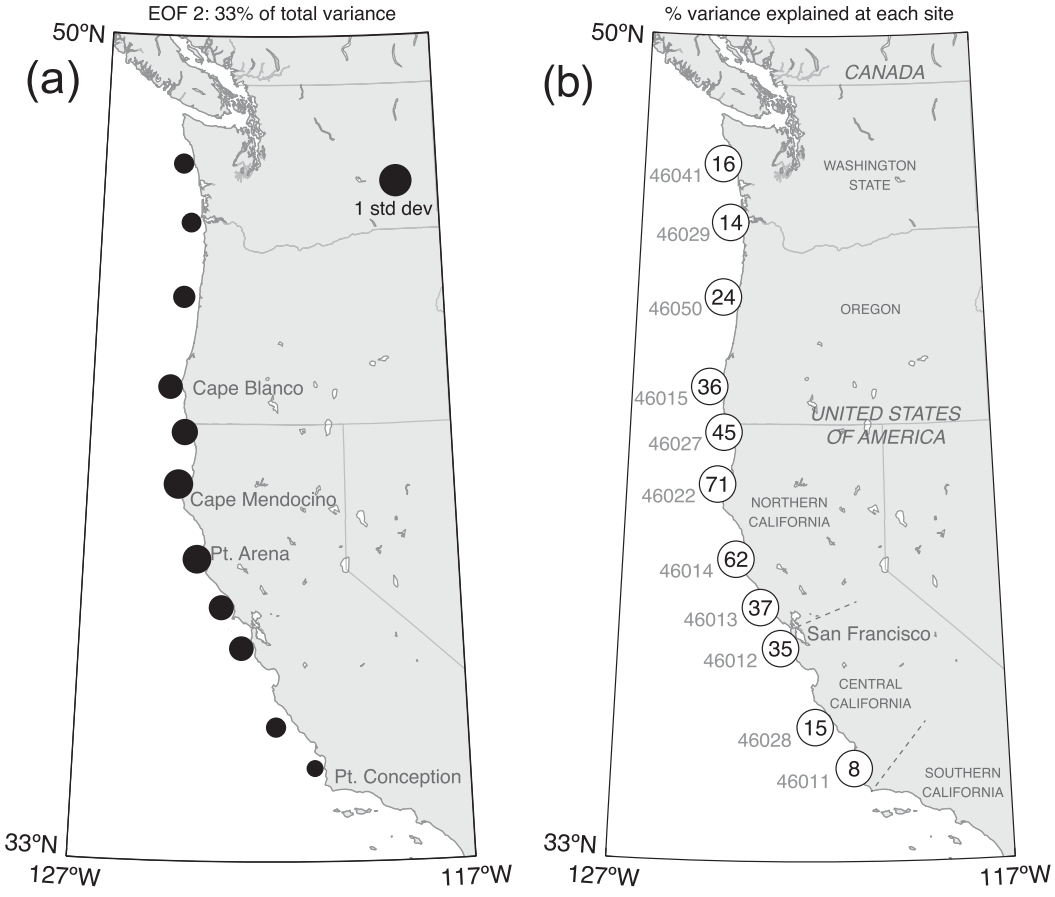

FIG. 5. As in Fig. 4, but for EOF 2.

fluctuations (Fig. 8f). The poleward propagation cannot be captured in a single standard EOF. The sum of EOFs 1 and 2 is a far better representation of the wind velocity fluctuations, in particular the poleward propagation of those fluctuations, than EOF 1 alone.

Overall, the EOF analysis tells us that much of the synoptic variance in the buoy winds is in a single dipole-like pattern (Fig. 4a). The partial coherence of EOFs 1 and 2 indicates that ~55%–60% of the along-coast wind velocity variance in the CCS should be describable in a single propagating pattern: 44% variance captured by EOF 1 + 0.4 × (33% variance captured by EOF 2). The pattern should be primarily a dipole but with some phase lag of propagation along the coast. In section 4, this pattern is identified with Hilbert EOF analysis.

4. A large-scale propagating structure in the buoy and satellite winds

The leading Hilbert EOF captures ~60% of the total synoptic wind velocity variance in summer over the CCS (Fig. 9), consistent with the prediction based on the regular EOFs at the end of the previous section. The Hovmöller diagram of HEOF 1 from either the buoy or QuikSCAT winds is very similar to the Hovmöller diagram of standard EOF 1 + 2 (Figs. 8c–e). The first HEOF mode captures ~40%–80% of the variance at each site along the coast, explaining more variance in the northern part of the CCS but still about half the variance in the southern part (Fig. 10a). The spatial phase pattern of HEOF 1 indicates that the wind velocity fluctuations are nearly in phase over the northern part of the CCS, ~42°–48°N, from Cape Blanco through Washington State (Fig. 10c). In contrast, the wind fluctuations in the southern part of the CCS, ~34°–40°N, propagate poleward, indicated by a phase shift that increases approximately linearly with latitude (Fig. 10c). As a result, the wind fluctuations at the north and south ends of the CCS are substantially out of phase (Fig. 10c, upper and lower ends), consistent with the dipole mode being the leading standard EOF in section 3.

The second HEOF captures ~25% of the total variance (Fig. 9). HEOF 2 is relatively unimportant in the northern part of the CCS, explaining ≤30% of the

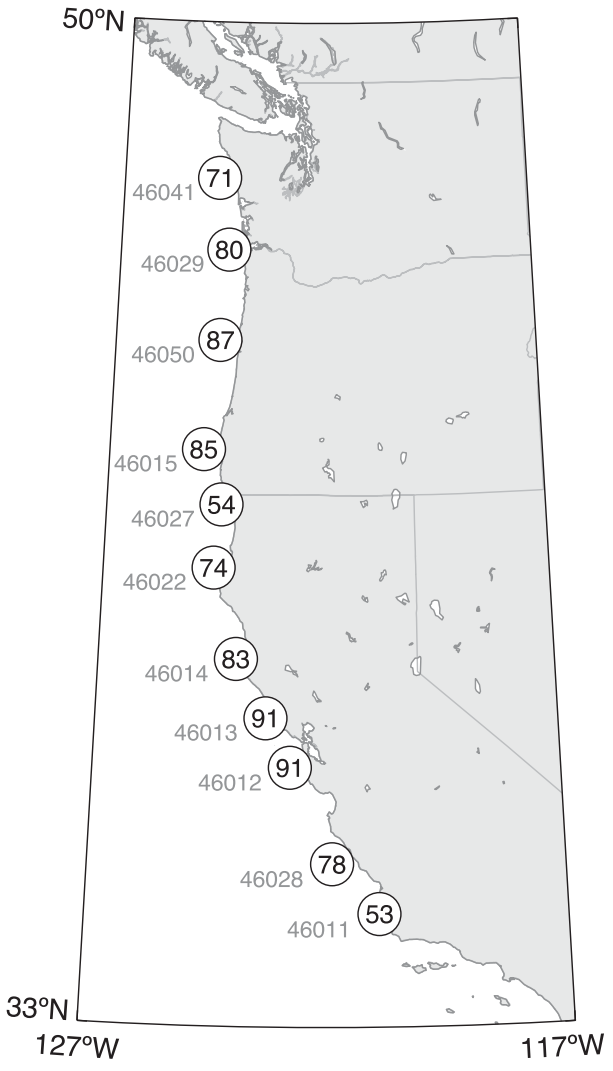

FIG. 6. Along-coast wind velocity variance explained at each buoy by the sum of EOFs 1 and 2, which together explain 77% of the total variance.

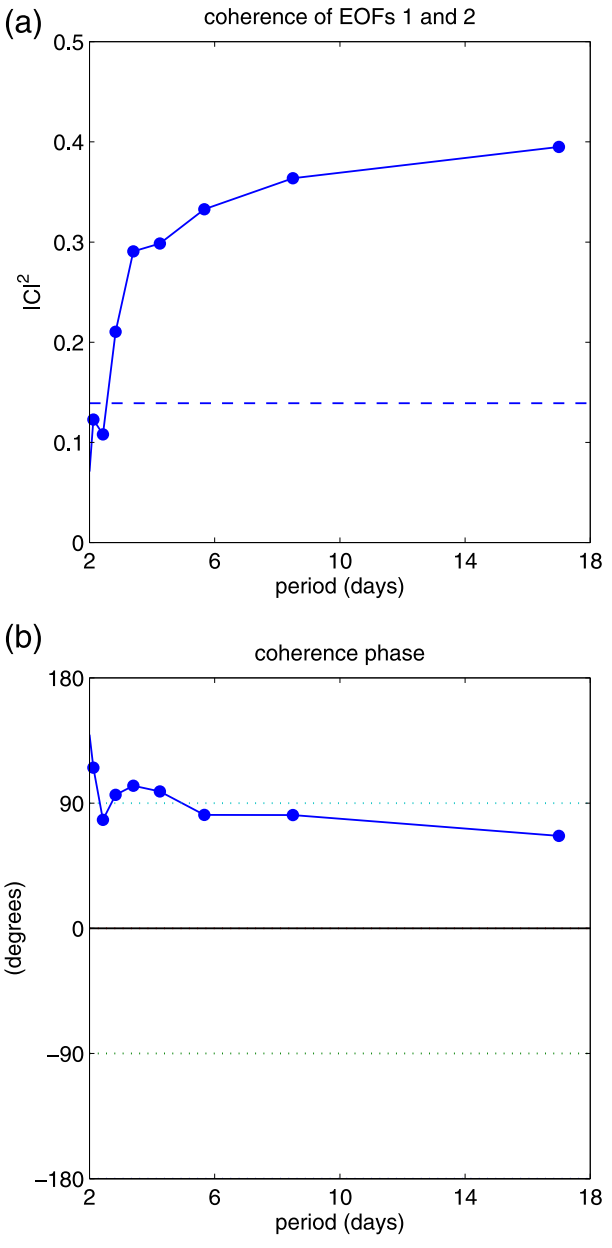

FIG. 7. Coherence of EOFs 1 and 2 of along-coast wind velocity from the 11 NDBC buoys. (a) Magnitude squared coherence. Dashed line indicates 95% significance level. (b) Coherence phase. The horizontal axis begins at a period of 2 days due to the $(48\,\mathrm{h})^{-1}$ low-pass filter that was applied to remove the diurnal cycle (section 2).

variance north of ~40°N (Fig. 10d), but explains up to half of the variance at some sites in the southern part of the CCS (Fig. 10d). The fluctuations captured by HEOF 2 are in phase over the southern half of the CCS (Fig. 10f). The phase shift in the central and northern CCS (Fig. 10f, upper half) is not very meaningful since HEOF 2 captures little wind velocity variance at those sites (north of ~40°N, Fig. 10d).

The consistency between the buoy and satellite results is better for the spatial phase (Figs. 10c,f) than the amplitude (Figs. 10b,e) or variance captured (Figs. 10a,d). The spatial phase patterns of HEOFs do tend to be more robust than the spatial amplitude patterns, due in part to array size effects (Merrifield and Guza 1990), which are further addressed below. In spite of differences in the spatial amplitude patterns, however, both the satellite and buoy data show that the dominant pattern of wind variability in the CCS in summer involves nearly out-of-phase fluctuations at the poleward and equatorward ends of the CCS (Fig. 10c).

The spatial phase patterns (Figs. 10c,f) are also robust to changes in the details of the HEOF calculation. Changing the minimum data chunk length for the buoy

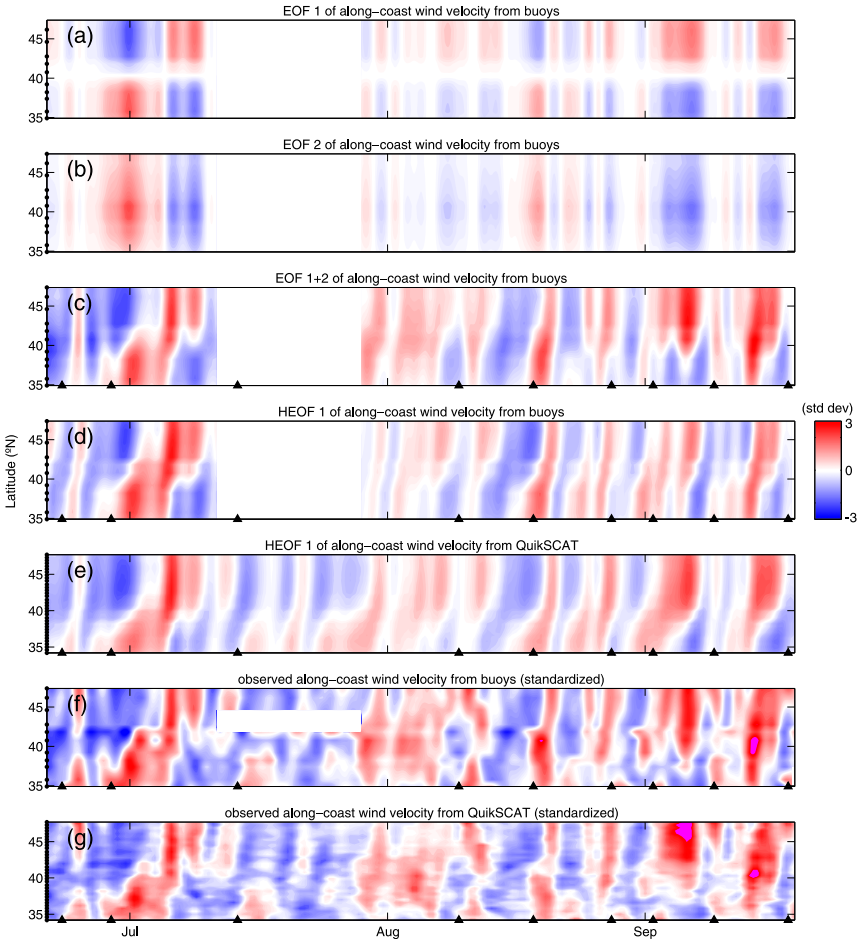

FIG. 8. (a)–(g) Hovmöller diagrams of along-coast wind velocity and its (H)EOFs during 21 Jun to 18 Sep 2009 (dates based on buoy data availability). In (d) and (e) only the real part of HEOF 1 is shown (see end of section 2e). In (f) and (g), the observed time series at each site has been scaled by its standard deviation to be consistent with the (H)EOFs. The color scale is the same in all panels and has units of standard deviations (at each site). Magenta areas in (f) and (g) indicate out-of-range positive values. Black dots on left axes indicate the positions of the buoys or QuikSCAT grid points. Black triangles along the horizontal axes indicate the times of onset of wind relaxation at Point Conception, CA, based on the Melton et al. (2009) index.

time series from 20 days to any value between 15 and 40 days, or varying which buoys are included along the CCS (as long as the buoys span most of the CCS and are roughly equally divided between the north and south), or changing the latitude limits of the QuikSCAT data range by a few degrees, changes the percent variance captured at each site in HEOF 1 (Fig. 10a) by $O(10\%)$, but the spatial phase patterns remain similar to Fig. 10c. The changes in either the QuikSCAT or buoy HEOF results from changing these details of the analysis are about the same size as the difference between the QuikSCAT and buoy HEOF results in Fig. 10.

The results are also not very sensitive to high- or low-pass filtering the QuikSCAT time series before calculating the HEOFs. With a high-pass filter, with any cutoff frequency less than $\sim(25\,\text{days})^{-1}$, the results are very similar to Fig. 10. With a low-pass filter, there is no substantial departure from the spatial phase patterns in Fig. 10 as long as the cutoff frequency is greater than $\sim(12\,\text{days})^{-1}$. (With a lower-frequency cutoff for that filter, the result is that the phase shift between the north and south ends of the CCS in Fig. 10c becomes closer to 180°.) Therefore, the time scales that are dominating the results in Fig. 10c are periods of ~10–25 days. With a 10–25-day bandpass filter applied before calculating the HEOFs, almost 70% of the variance is captured by the first HEOF, as compared to the ~60% shown in Fig. 9.

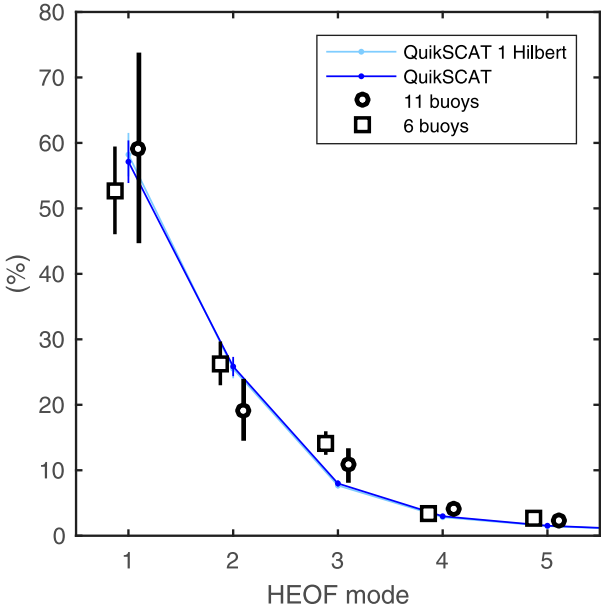

FIG. 9. Eigenvalue spectra, indicating the percent of the total along-coast wind velocity variance captured by Hilbert EOFs 1–5 using data from buoys and from QuikSCAT. Vertical bars are 95% confidence interval estimates following North et al. (1982) (see section 2e); in some cases, the bars are smaller than the symbols. In legend, "11 buoys" indicates the full set of buoys shown in Fig. 1, and "6 buoys" indicates the subset of buoys used to extend the HEOF results back to the period covered in Mass and Bond (1996) (see section 2g). For clarity, the buoy results are slightly offset horizontally.

HEOF spatial amplitudes can be distorted by observational array size effects (Merrifield and Guza 1990), but those effects should not be strong here. For HEOF analysis to successfully detect propagating signals that may be irregularly spaced in time, such as these wind relaxations and intensifications, Merrifield and Guza (1990) find the requirement

$$\Delta k \le \overline{k}, \tag{18}$$

where Δk is the wavenumber bandwidth of the signal of interest and $\overline{k}$ is the mean wavenumber in the band. Making the approximation that the signal is nondispersive, so $\Delta k = \Delta\omega/c$, where c is the phase speed and ω is the angular frequency, this requires $\Delta\omega \le \overline{\omega}$. Using $\omega = 2\pi/T$ where T is the period, this requires

$$\omega_2 - \omega_1 \le \overline{\omega}, \tag{19}$$

$$\frac{2\pi}{T_2} - \frac{2\pi}{T_1} \le \frac{1}{2}\left(\frac{2\pi}{T_2} + \frac{2\pi}{T_1}\right). \tag{20}$$

Because the spatial phase pattern is robust to array size effects (Merrifield and Guza 1990), we can use the information from the filtering sensitivity analyses in the previous paragraph to determine that the period band of the dominant signal is ~10–25 days, so $T_1 = 25$ days and $T_2 = 10$ days (T_2 is the period corresponding to the higher frequency). The Merrifield and Guza (1990) requirement in Eq. (20) above is satisfied for this period band. This requirement is related to the array size ΔX in two ways (Merrifield and Guza 1990). The first is that the longest effective observing array size is $\Delta X_{\text{eff}} \approx 2\pi/\Delta k$. The array used here is the 1600-km buoy and QuikSCAT observation line along the CCS (Fig. 1). Therefore, again using $\Delta k = \Delta\omega/c$, the definition of ΔX_{eff} implies that in the 10–25-day band the present HEOF analysis will be effective for signals with phase speeds $\gtrsim$96 km day^{-1}. The second relation is the requirement $\Delta X_{\text{eff}} \gtrsim 2\pi/\overline{k}$, which goes into the derivation of Eq. (18) above. To satisfy this, the phase speed c of the CCS signals must be $\lesssim$112 km day^{-1}. These two requirements are also roughly met, since for the central frequency in this band, equivalent to a period of ~15 days, with a wavelength equivalent to the 1600-km CCS the phase speed is ~110 km day^{-1}. Therefore, the array size effects that can distort HEOF spatial amplitude patterns for signals with large bandwidth (Merrifield and Guza 1990) should not be severe in this HEOF analysis. Regardless, the focus here is less on the spatial amplitude pattern than on the more robust spatial phase pattern.

Overall, the HEOF analysis indicates 1) substantial coherence in wind velocity fluctuations across the entire CCS (Fig. 10a), 2) a temporal lag between the wind fluctuations in the north and south parts of the system, separated at ~40°N (Fig. 10c), and 3) nearly out-of-phase wind fluctuations in the north and south ends of the CCS (Fig. 10c, upper and lower ends).

5. Large-scale structure is muted in lagged correlations between buoy pairs

a. Lagged correlation of wind at buoy pairs

Correlations of wind velocity at pairs of buoys are qualitatively consistent with the leading EOF and HEOF presented above, showing a split between the north and south parts of the CCS. For example, the wind velocity at buoy 46011 off central California is significantly correlated with wind at all 10 other buoys, indicating significant large-scale coherence across the entire system (Fig. 11a, arrows). The sign of the correlation is consistent with the EOF 1 and HEOF 1 modes: negative for buoys poleward of Cape Mendocino and positive for buoys equatorward of Cape Mendocino. However, the variance explained is less than the variance captured by EOF 1 or HEOF 1 in the previous sections. For buoys in the poleward part of the system,

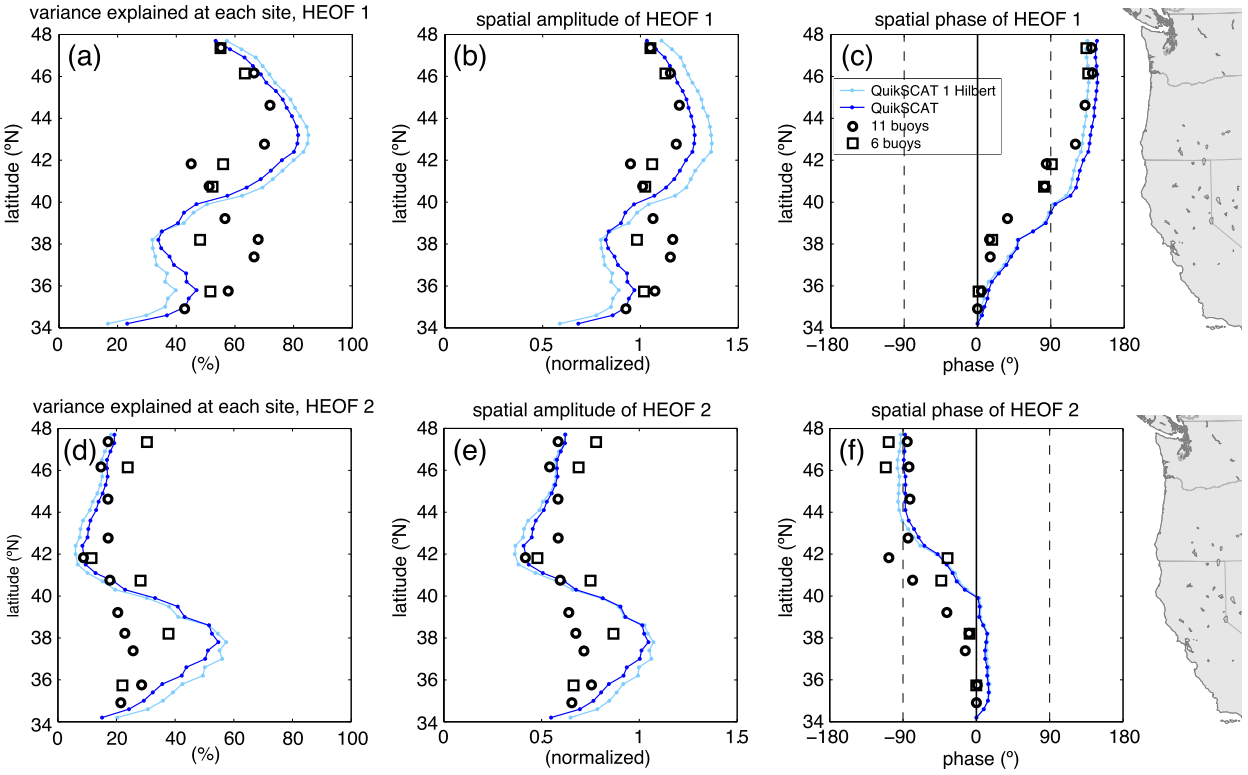

FIG. 10. (a)–(f) Spatial patterns of HEOFs 1 and 2 of along-coast wind velocity from buoys and from QuikSCAT satellite vector wind data. HEOFs 1 and 2 explain 55%–60% and 20%–25% of the total variance, respectively (Fig. 9). In (b) and (e) the normalized amplitudes have units of the standard deviation of wind velocity at each site.

the pairwise correlation with buoy 46011 is $|r| \sim 0.4$ or smaller. For buoys south of Cape Mendocino, $|r| = 0.4$–0.8 with time lags of 0–1 day.

Using a reference buoy in a different location off central California, or off Washington, gives results consistent with Fig. 11a. Correlations of winds off central California are somewhat higher with reference buoy 46028 instead of 46011 (Fig. 11b), as expected for buoys closer together in space. Buoys 46029 at the Washington/Oregon border (Fig. 11c) and 46041 off northwest Washington (not shown) give equivalent results, with the sign of the lag between the poleward and equatorward regions reversed compared to Figs. 11a and 11b as expected (Fig. 11c). Depending on the reference buoy, buoy 46022 near Cape Mendocino has a maximum correlation at negative or positive lag, indicating wind fluctuations near Cape Mendocino are related to fluctuations in both the north and south regions. However, the correlation is low between buoy 46022 and other buoys, and the difference between the correlations of 46022 with northern versus southern buoys is not statistically significant. Overall, regardless of reference buoy, there is a lag of 1–1.5 days between wind velocity in the poleward and equatorward regions of the CCS, and poleward propagation with a time scale of 0.5–1 day within each region.

b. *Impact of landfalling fronts on correlations versus EOF analysis*

Why do the correlations between buoy pairs not capture as much variance as the (H)EOF analyses (section 5a)? This may be because landfalling fronts affect the two types of analysis differently. Lagged correlation analysis involves the wind at buoy pairs only. The landfalling fronts typically are not large enough to span the entire coastline from Washington to central California (Halliwell and Allen 1987). However, the strong wind velocity variance characteristic of fronts may cause the frontal events to dominate the lagged correlation analysis between pairs of nearby buoys. In contrast, EOF analysis emphasizes wind fluctuations that are coherent across all the buoys. Therefore, fronts should not dominate the EOF analysis when a whole-coast pattern of variability exists. For this reason, EOFs or HEOFs are a better tool than pairwise correlation for revealing large-scale coherent patterns in the wind field.

Landfalling fronts are also a plausible explanation for why the along-coast time lags in the correlations

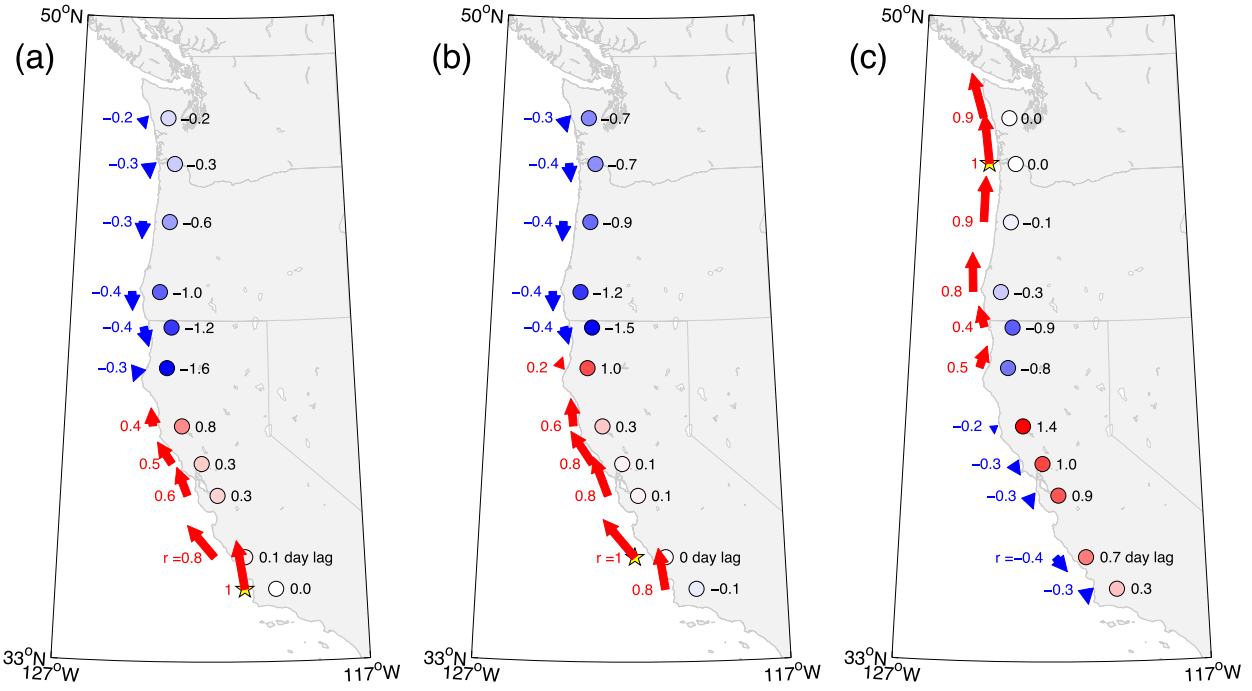

FIG. 11. Maximum lagged correlation between wind velocity time series at pairs of buoys. At each location, an arrow indicates the correlation coefficient r of the along-coast wind velocity at that buoy with reference buoy (a) 46011, (b) 46028, or (c) 46029. Yellow star indicates the reference buoy. Blue and red arrows indicate negative and positive r, respectively, with $r = 1$ at the reference buoy. The r value is shown to the left of each arrow. Colored circles indicate the lag that gives maximum correlation; the lag value is shown to the right of each circle. Positive lag indicates wind fluctuations at that buoy follow fluctuations at the reference buoy.

between buoy pairs, at most 1.5 days, are different than the time lags implied in the leading (H)EOF mode: several days or more between the northern and southern CCS for a ~140° phase lag in a synoptic wind pattern with a ~10-day or longer cycle such as discussed in section 1. During frontal passage, the wind can be in phase at neighboring buoys that during wind relaxations have a phase lag (e.g., Mass and Bond 1996). Further, when an eastward-propagating front crosses the coastline at an angle, the apparent along-coast phase propagation can be poleward, zero, or even equatorward, opposite to the phase propagation during wind reversals (Halliwell and Allen 1987; Nuss et al. 2000) or relaxations (Fewings et al. 2016). Therefore, for time lag between pairs of buoys, there are at least two classes of events. Some events are the three-stage relaxation or reversal events, with lags of several days. Fewer events are the landfalling fronts, with short lags of 0–1 day or negative lags. The lags identified by the correlation analysis here will be similar to a weighted average of the lags from these two classes of events. Although the landfalling fronts are fewer in number, the wind velocity variance during frontal events is strong. Fronts were removed from previous studies of wind relaxation and reversal off California (e.g., Mass and Bond 1996; Fewings et al. 2016). Landfalling fronts likely have a greater influence than the three-stage event sequences on the pairwise correlation analysis, causing it to yield shorter average lags of 0–1 day. The EOF and HEOF analyses are likely less sensitive to fronts and reveal the dominant large-scale structure, with most energy at time scales of several days and longer.

6. Relating the large-scale wind structure to previous studies

a. *Interpreting the large-scale structure in the context of the three-stage wind event cycle*

The quasi-dipole structure in the summer wind variability over the CCS that is captured in HEOF 1 is related to the three-stage event sequence that dominates summer wind variability in the CCS described in section 1. This can be seen by considering composite averages of the time series of HEOF 1 near the north and south ends of the CCS, composited over previously identified times of wind relaxations or reversals identified as described in section 2j (Figs. 12–14). Although the event indices used for compositing are indices of stage 3 of the event sequence, stages 1 and 2 are also visible in the results, as follows.

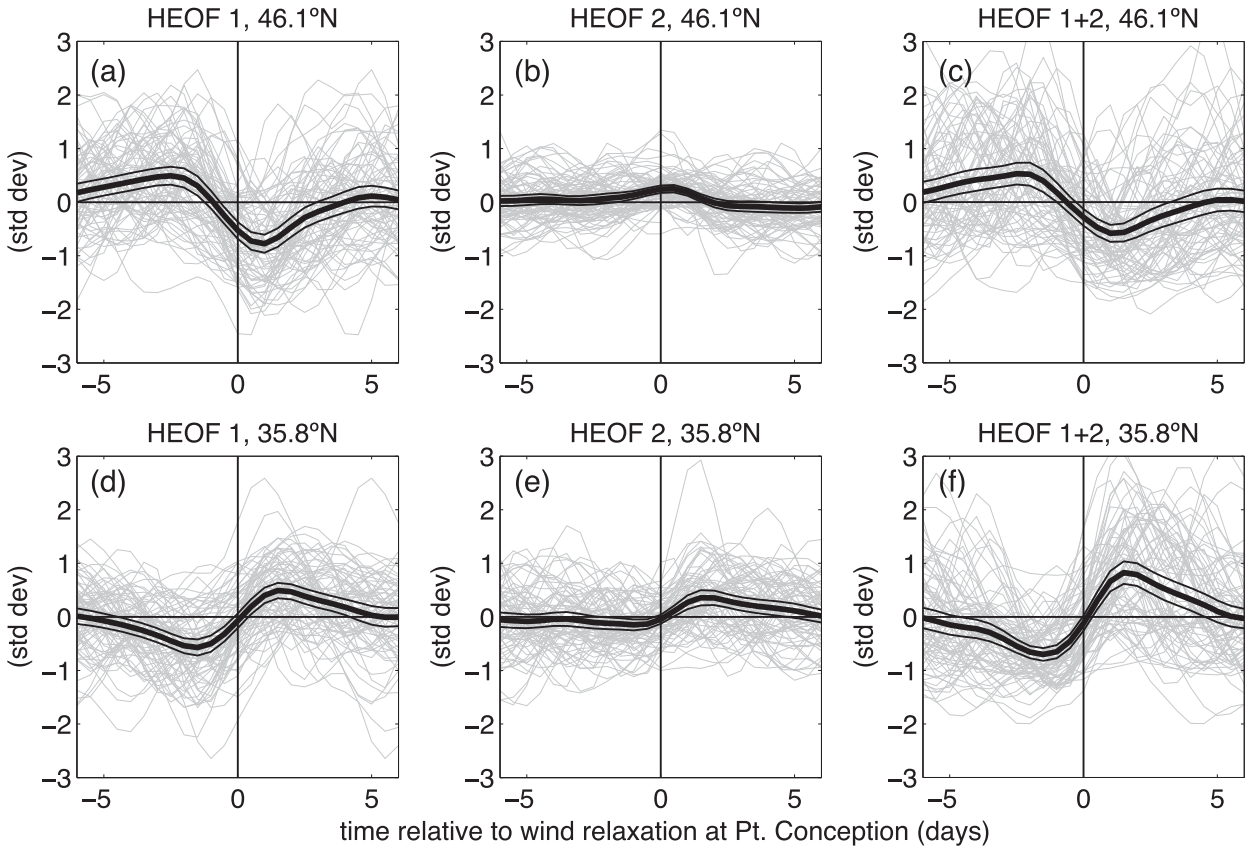

FIG. 12. Composite averages of the leading HEOFs of wind velocity during 82 known wind relaxations near Point Conception, CA, during June–September 2000–09. The time series of the HEOFs from QuikSCAT along-coast wind velocity are shown (real part only). The top and bottom rows show time series off the Washington–Oregon border and central California (near buoys 46029 and 46028), respectively, from 6 days before to 6 days after the onset of wind relaxation. The vertical black line in each panel indicates the onset of wind relaxation at Point Conception ($t = 0$), identified following Melton et al. (2009) (see section 2j). Thin gray lines show HEOF time series surrounding individual relaxation events. Thick and thin black lines show the mean over all events and a 95% confidence interval around the mean. Positive indicates poleward wind velocity fluctuation (wind relaxation) and negative indicates equatorward wind velocity fluctuation (intensified upwelling-favorable wind). The real part of (a),(d) HEOF 1; (b),(e) HEOF 2; and (c),(f) HEOF 1 + 2 is shown. The amplitudes are normalized as discussed in section 2f and have units of the standard deviation of wind velocity at each site.

Stage 1 of the wind event cycle consists of wind relaxation or reversal at the northern end of the CCS, and is visible in HEOF 1. During the several days previous to the onset of a southern wind relaxation or reversal (vertical black lines in Figs. 12, 13), HEOF 1 is positive in the northern CCS (Figs. 12a, 13a, left side), indicating wind relaxation or reversal in the northern CCS. This is consistent with the stage 1 wind relaxations or reversals off Oregon that were previously linked to wind relaxations and reversals at Point Conception in the southern CCS, but preceded the Point Conception relaxations by several days (Fewings et al. 2016).

Stage 2 of the wind event cycle is also captured in HEOF 1. During the ~2 days before the known wind relaxations and reversals at the south end of the CCS (vertical black lines in Figs. 12–14), HEOF 1 tends to be negative in the southern CCS (Figs. 12d, 13d and 14a, left sides). Negative HEOF 1 represents intensified upwelling-favorable wind. Therefore, these negative fluctuations in the southern end of the CCS are consistent with stage 2 of the previously described wind event cycle (Melton et al. 2009; Fewings et al. 2016). Also consistent with stage 2, during the time when the southern CCS wind relaxation is beginning, in the northern CCS HEOF 1 is negative (Figs. 12a and 13a, day 0–1), indicating intensified upwelling-favorable winds. This is consistent with the timing of stage 2 of the wind event cycle in Halliwell and Allen (1987) and Fewings et al. (2016).

Stage 3 of the event cycle consists of wind relaxation, or rarer reversal, in the southern part of the CCS (Fewings et al. 2016). Positive fluctuations of HEOF 1, which indicate poleward wind velocity fluctuations, tend to begin at the relaxation times identified by Melton

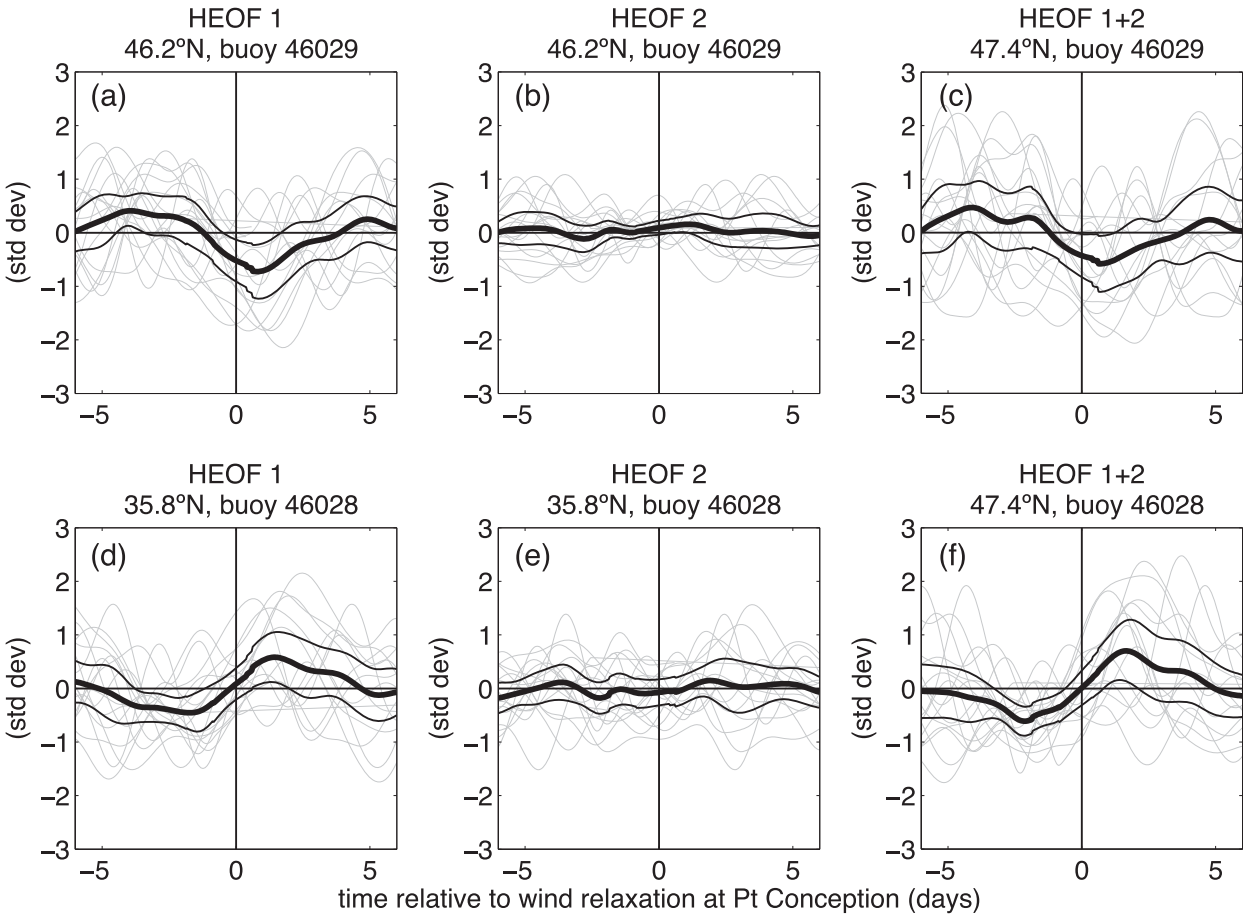

FIG. 13. As in Fig. 12, but for HEOFs from the 11 buoys composited over 17 known wind relaxations near Point Conception, CA, during June–September 2003, 2004, 2009, 2011, and 2016 identified following Melton et al. (2009). The top and bottom rows show time series off the Washington–Oregon border and central California from buoys 46029 and 46028, respectively.

et al. (2009) (Figs. 8d,e, black triangles; Figs. 12d, 13d, time 0 and onward). Some of the positive fluctuations of HEOF 2 likewise follow these wind relaxation events (Figs. 12e, 13e), but most of the signal associated with the wind relaxations at Point Conception is captured by HEOF 1 (cf. Figs. 12d,e,f; most of the signal in Fig. 12f comes from Fig. 12d). These wind relaxations at Point Conception constitute stage 3 of the wind event cycle and are captured in HEOF 1 as positive fluctuations in the southern end of the CCS. Further supporting this relation of HEOF 1 to the known wind event cycle, positive fluctuations of HEOF 1 are associated with the start of the wind reversals off central California identified by Mass and Bond (1996) and Bond et al. (1996) (Fig. 14a, day 0–1). These events constitute a stronger subset of the events associated with stage 3 of the wind event cycle, a subset in which small-scale coastal processes involving the marine boundary layer strengthen a wind relaxation or reversal that is initiated by the synoptic-scale forcing (Mass and Bond 1996).

Together, the composite averages of HEOF 1 over the wind relaxations identified in Melton et al. (2009) (Figs. 12a,d) indicate that positive fluctuations in the poleward and equatorward ends of the wind quasi dipole (HEOF 1) can be interpreted as stage 1, the wind relaxation/reversal off Oregon, and stage 3, the wind relaxation off central California that follows. The stage 3 wind anomalies are known to propagate poleward over the south part of the system (e.g., Nuss et al. 2000; Fewings et al. 2016), consistent with the increasing phase lag with increasing latitude off central California in Fig. 10c. Negative fluctuations of HEOF 1 in either end of the system represent stage 2, the intervening wind intensification, which also propagates poleward (e.g., Figs. 4 and 6 of Fewings et al. 2016).

The spatial phase from the Hilbert EOF analysis indicates poleward propagation of wind fluctuations (Fig. 10c). This poleward sense of propagation is consistent with the Hovmöller diagrams of observed wind velocity (Figs. 8f,g) and with previous studies, as discussed

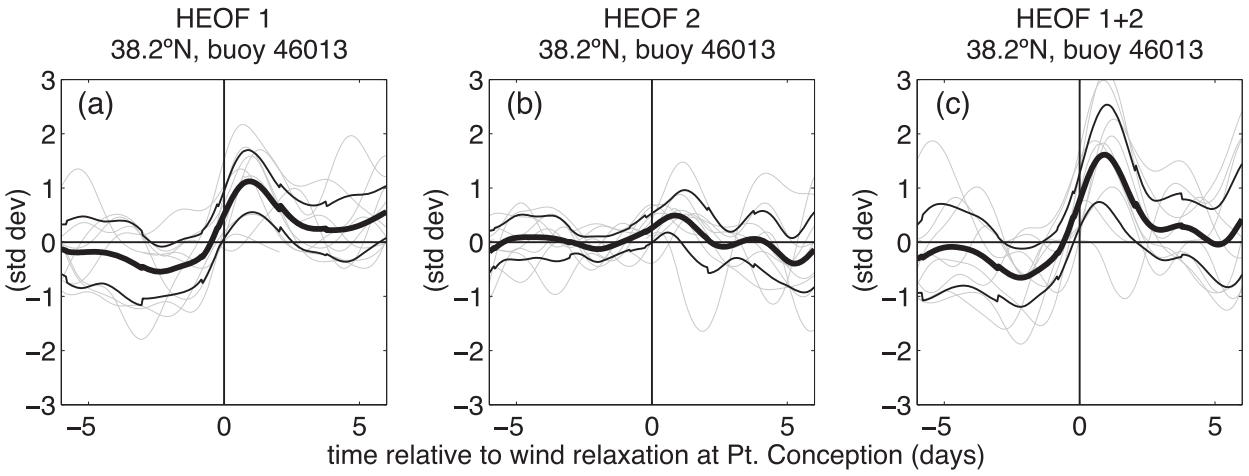

FIG. 14. As in Fig. 13, but for buoy HEOFs from a reduced set of buoys (46041, 46029, 46027, 46022, 46013, and 46028) composited over 12 known wind reversals identified in Table 1 of Bond et al. (1996) and Table 2 of Mass and Bond (1996) at buoy 46013 off California during June–September 1984, 1985, 1987, and 1989. The small jumps in the black curves are because the HEOF time series are not available for the entire 12-day window surrounding each of the 12 events.

above. However, the three-stage event sequence could suggest equatorward propagation: relaxation off Oregon, followed a few days later by relaxation off California; and HEOF 1 is also consistent with that three-stage sequence (Figs. 12, 13, as described above). This seems puzzling, but a plausible explanation is that the positive phase lag of the northern part of the CCS relative to the southern part in Fig. 10c represents the beginning of another event cycle. Because the event cycle repeats throughout the summer, the Oregon relaxation, which is stage 1 of a given wind event cycle, must follow stage 3 of the previous cycle. This is supported by Fig. 6 of Fewings et al. (2016), in which a second wind relaxation off Oregon is visible 5 days after the onset of the central California relaxation, presumably indicating the beginning of the next three-stage event cycle. Apparently, the three-stage event sequence described above that repeats as stages 1–2–3–1–2–3–1–2–3… is captured by HEOF 1 as stages 2–3–1–2–3–1–2–3–1…. Because the sequence repeats, there is no preferred beginning stage for the sequence. Viewed in this way, the three-stage event sequence is consistent with the poleward propagation identified in the HEOF analysis.

The spatial phase lag of HEOF 1 across the CCS and the time lag between the northern and southern wind relaxations in the composite averages (Figs. 12a, 13a) also support the idea that HEOF 1 is mainly capturing the three-stage wind relaxation and intensification cycle. The phase lag of ~140° of the wind fluctuations off central California relative to wind fluctuations off the Pacific Northwest in HEOF 1 (Fig. 10c) apparently corresponds to an average time lag of ~4 days (Figs. 12a,d), suggesting the propagating signals are dominated by periods of ~10 days [=(4 days) × 360°/140°]. This period is consistent with the ~10–12-day event cycle shown in Fewings et al. (2016).

b. *Reconciling the large-scale structure with the shorter spatial decorrelation scale for wind*

How can the quasi-dipole pattern captured by the buoy EOFs and the HEOFs, which spans the entire ~1600-km CCS, be reconciled with the 400–800-km along-coast decorrelation scale for wind velocity (Halliwell and Allen 1987)? Presumably, landfalling fronts would affect that correlation analysis similarly to the correlation analysis here (section 5b). Additionally, Cape Mendocino is the node of the dominant dipole EOF wind pattern (Fig. 4a), so we should not expect a good correlation between winds there and in other parts of the system, even though winds north and south of Cape Mendocino are correlated with each other (section 5a). Indeed, the correlation analysis in Halliwell and Allen (1987, their Fig. 6), which is similar to Fig. 2 in this paper, is consistent with a quasi-dipole structure centered at Cape Mendocino: the correlation of wind velocity at pairs of buoys drops to zero near Cape Mendocino and becomes negative for buoy pairs separated by Cape Mendocino. The existence of the node in the dominant wind pattern (Fig. 4a) reduces the apparent along-coast correlation scale between buoy pairs. Equivalently, the existence of a phase difference between winds at buoys separated by Cape Mendocino near 40°N (Fig. 10c) leads to a low correlation at zero lag.

c. *Reconciling the large-scale structure with previous EOF analyses*

Earlier EOF analyses of synoptic wind variability in the CCS in summer (section 1) did not show a dipole

mode as the dominant wind velocity pattern, unlike the buoy EOF analysis presented here (Fig. 4). Those studies instead found a dipole as the second EOF. There are multiple explanations for this. First, several of the previous studies had a smaller latitudinal extent. One focused on the northern part of the CCS, ~41.5°–47°N (Samelson et al. 2002). Another examined 40°–48°N (Perlin et al. 2004). In those cases, the leading EOF was not a dipole mode likely because the study domains were within the northern half of the dipole presented in Fig. 4. Therefore, the results were dominated by the northern half of the dipole in Fig. 4a, making the leading EOF unidirectional. Reducing the buoys or QuikSCAT data in the present study to a subset covering only the northern half of the domain, or not including buoys 46011 and 46028, gives a similar result (not shown).

Second, the distribution of study sites within the domain can affect the results. Another previous study included the southern and central parts of the domain considered here (35°–41.5°N; Kelly 1985) but had many more sampling locations near 38°–39°N than to the north or south, which is likely to weight the resulting EOF toward the wind patterns in the center of the CCS. These effects of study domain extent and sampling distribution are consistent with the suggestion in Perlin et al. (2004) that the differences in that study versus Kelly (1985) were because the two studies emphasized sites north and south of Cape Mendocino, respectively. Therefore, one reason the dipole mode was not previously recognized as the dominant EOF mode of wind variability in summer in the CCS is that prior analyses focused on regions smaller than the spatial extent of the dipole mode (Fig. 4a), causing one part of the dipole mode to emerge as the leading standard EOF.

Third, the dominant structure in the wind fluctuations changes seasonally. The character of the midlevel forcing and resulting wind variability over the CCS has a strong seasonal dependence (e.g., Hickey 1979; Halliwell and Allen 1987). The present study focuses on summer, as did Kelly (1985), Samelson et al. (2002), and Perlin et al. (2004), though Kelly (1985) also included April and May, which may contribute to the differences between that study and the present study. In contrast, Castelao and Wang (2014) included all months of the year, but also found the dipole mode as the second EOF. Here, if the EOF analysis is repeated using all times of year, the dipole is also no longer the first mode (not shown), presumably because larger-scale winter storms and fronts dominate the annual wind variability and individual storms affect larger regions of the coastline in winter than in summer.

Fourth, the satellite and buoy wind data do not always give the same result regarding whether the dipole is the leading EOF, and the solution is to recognize that the first two standard EOFs are related. Two of the previous studies of summer winds also used QuikSCAT data (Samelson et al. 2002; Perlin et al. 2004), and one used buoy data (Kelly 1985). In the present analysis, the satellite data yield a dipole as the leading EOF mode when QuikSCAT data from only the locations nearest the buoys are used (not shown). But when the data along the entire QuikSCAT line in Fig. 1 are included, the dipole is no longer the first EOF mode or is very asymmetric, with the node near one end of the CCS (not shown). Therefore, details of the choice of sampling sites even within the QuikSCAT line apparently can cause variance to move between standard EOFs 1 and 2. This lack of robustness in the EOF results is not meaningful, however, because 1) for both the buoys and QuikSCAT, EOFs 1 and 2 are partially correlated at nonzero time lag, due to the propagation of the wind fluctuations (section 3c), and 2) buoy EOFs 1 and 2 have degenerate eigenvalues (section 3b). The apparently discrepant standard EOF analysis results from buoys and QuikSCAT are unified by the Hilbert EOF analysis, which isolates in a single HEOF mode the propagating variance that was split between two EOF modes and gives consistent results for the buoys and QuikSCAT (e.g., Figs. 9, 10c). A sensitivity analysis with various site groupings indicates the HEOF results are similar for buoy and QuikSCAT winds in all cases where the sites span the coastline from Washington through central California and are roughly evenly distributed across the system (Fig. 10 and other cases not shown for simplicity). The time series of the HEOFs from the various cases are also very similar (not shown). Because the standard EOFs 1 and 2 are partially coherent (section 3b), the CCS wind field is better represented with HEOFs than standard EOFs.

Overall, when the analysis spans the entire CCS and uses Hilbert EOFs, much of the summer wind variability in the CCS along the coast is captured in a single mode with substantial phase difference between the north and south parts of the system. In contrast, with standard EOF analysis this variability is split between two modes that are related (section 3b). Therefore, Hilbert EOFs are better for characterizing the wind field since it has propagating variability. Although previous results using regular EOFs suggested the leading mode of wind variability was unidirectional, the HEOF analysis shows an essential out-of-phase character in the fluctuations in the northern and southern ends of the CCS.

7. Implications of the large-scale structure in wind forcing over the CCS

By including sites that span the entire CCS coastline, and using an analysis technique that allows for propagation in the wind velocity fluctuations, this analysis revealed that ~60% of the synoptic wind variability in summer over the CCS is in a coherent pattern that spans the entire ~1600-km coastline and is nearly out of phase in the north and south ends of the system (sections 3 and 4). What are the implications for our understanding of wind forcing over the California Current System during the summer upwelling and relaxation season?

First, we should use caution when interpreting the mean wind pattern. The time-mean wind field in the CCS is a single area of intensified upwelling-favorable wind stress extending from Washington State past Point Conception, California [Nelson (1977); e.g., see Fig. 4 of Fewings et al. (2016)]. However, the analyses presented here suggest the time mean is not a good representation of the wind forcing. The wind tends not to be intense simultaneously over the entire system. If that were so, the first EOF mode would have a uniform spatial pattern, and the first HEOF would have a constant spatial phase over the entire CCS, very different from the dipole and quasi-dipole modes described in sections 3a and 4. The fact that the poleward and equatorward parts of the CCS are not in phase in the leading HEOF mode (Fig. 10c) indicates that winds in the poleward and equatorward parts of the CCS tend not to be intensified, or relaxed, simultaneously. Rather, the wind fluctuations in the poleward and equatorward areas are closer to alternating in time (Fig. 12a versus Fig. 12d).

Second, there are implications for the cross-shelf ocean circulation, the resulting coastal upwelling, and its forcing of the CCS ecosystem. The nearly out-of-phase wind forcing in the north and south ends of the CCS (Figs. 10c, 12) may lead to an out-of-phase structure in coastal upwelling of cold water (Kelly 1985) and nutrients (e.g., Hales et al. 2005a); uptake of carbon dioxide from the atmosphere (Hales et al. 2005b); offshore export of nutrients and phytoplankton in the surface boundary layer (Evans et al. 2015); and near-bottom cross-shelf transport of particulate organic matter (Karp-Boss et al. 2004; Hales et al. 2006) and low-pH, low-oxygen water that can lead to hypoxia on the continental shelf (Grantham et al. 2004; Chan et al. 2008; Connolly et al. 2010; Siedlecki et al. 2015).

Third, there are implications for regional ocean surface mixing and air–sea heat fluxes. These wind fluctuations generate substantial sea surface temperature (SST) and air–sea heat flux anomalies extending ~2000 km offshore (Flynn et al. 2017). The temperature anomalies are warm off the northern CCS but cold off the southern CCS. This asymmetry is due partly to the decrease in SST off central California caused by wind-driven mixing during the wind intensification (stage 2) that precedes southern CCS relaxations (stage 3). This cold preconditioning of SST prevents a warm SST anomaly during stage 3. The fact that the wind quasi-dipole leads to asymmetric SST anomalies in the northern and southern CCS suggests the wind quasi-dipole structure could be a factor in the greater cloudiness off the southern CCS (Flynn et al. 2017).

Fourth, the along-shelf ocean circulation will be affected both near the coast and over the open continental shelf and slope. Wind reversals and relaxations affect the nearshore coastal ocean by allowing poleward oceanic flow (e.g., Send et al. 1987; Melton et al. 2009; Washburn et al. 2011). Therefore, the wind forcing structure suggests there will be a pattern of alternating warm oceanic relaxation flows in the poleward and equatorward parts of the CCS. The along-coast wind stress is among the dominant driving forces for along-shelf flow, both over the inner shelf (e.g., Fewings et al. 2015) and the mid to outer shelf and slope (e.g., Winant et al. 1987), including generating coastal-trapped waves [reviewed by Brink (1991)]. The along-coast alternation in the winds has a time scale of ~10–25 days (section 4). The speed of oceanic coastal-trapped waves in the CCS is ~2.5 $m\,s^{-1}$ (e.g., Battisti and Hickey 1984). This is the same magnitude as the phase speed of these synoptic wind forcing patterns moving along the coastline: ~1600 km in ~10–25 days is ~1–2 $m\,s^{-1}$, suggesting the possibility of an oceanic coastal trapped wave being continuously forced by the large-scale wind anomalies as it propagates up the coast. Convergence in the along-shelf flow at capes due to the out-of-phase structure in wind forcing may affect the timing of the generation of mesoscale filaments and eddies (e.g., Kelly 1985; Perlin et al. 2004), which are important for exporting carbon and nutrients from the upwelling system (Renault et al. 2016).

It is unclear whether a similar quasi-dipole structure in wind variability will be present over other eastern boundary upwelling systems. In the CCS, the synoptic wind variability is strongly affected by the midlevel atmospheric forcing (Halliwell and Allen 1987), the low-pressure area over the nearby desert (Nuss 2007), and the coastline shape (Rogerson 1999; Edwards et al. 2002). In other eastern boundary upwelling systems, the relative importance of these three factors may be different. For example, in the Chile–Peru upwelling system, midlevel ridging also causes offshore advection of a desert heat low-pressure center and subsequent coastal wind relaxations (Garreaud et al. 2002), but there may not be a spatial pattern of out-of-phase wind relaxations at the other end

of the system because the coastline does not bend the same direction as at Cape Mendocino in the CCS. Using HEOFs to characterize the propagating wind variability and midlevel forcing in other eastern boundary systems could be a fruitful way to disentangle the effects of midlevel atmospheric forcing, advection of desert heat low pressure, and coastline shape on the coastal wind variability.

Acknowledgments. This study was supported by NASA Ocean Vector Winds Science Team Grant NNX14AI06G to the University of Connecticut (UConn) and NASA/California Institute of Technology, Jet Propulsion Laboratory Subcontract 1544398 to UConn. I thank Christopher Gotschalk [University of California, Santa Barbara (UCSB)] for continuing to update and share his MATLAB file of collected NDBC buoy data along the CCS and extending the Melton index forward in time; his time was partially supported by NSF OCE-1031893 and OCE-1232779: SBC-LTER III to UCSB. I also thank J. Tom Farrar [Woods Hole Oceanographic Institution (WHOI)] for suggesting the lagged regression analysis and Libe Washburn (UCSB), Kelly Lombardo and Craig Tobias (UConn), Steven Lentz (WHOI), LuAnne Thompson (University of Washington), Carlos Moffat (University of Delaware), and three anonymous reviewers for helpful comments on the manuscript. I incorporated some MATLAB code from Carlos Moffat (University of Delaware), Robert Beardsley (WHOI), Libe Washburn (UCSB), Clint Winant (University of California, San Diego), and Rich Signell (USGS). The wind velocity data are available at http://www.ndbc.noaa.gov, the coastline data at http://www.ngdc.noaa.gov/mgg/shorelines/data/gshhs, and the QuikSCAT satellite vector wind data at https://podaac.jpl.nasa.gov. The MATLAB toolboxes are available at http://www.eoas.ubc.ca/~rich/map.html for M_Map by Rich Pawlowicz (University of British Columbia) and http://www.cmar.csiro.au/datacentre/ext_docs/seawater.htm for SeaWater by Phil Morgan and Lindsay Pender of CSIRO (copyright Phil Morgan, 1993).

REFERENCES

Aristizábal, M. F., M. R. Fewings, and L. Washburn, 2016: Contrasting spatial patterns in the diurnal and semidiurnal temperature variability in the Santa Barbara Channel, California. *J. Geophys. Res. Oceans*, **121**, 427–440, doi:10.1002/2015JC011239.

——, ——, and ——, 2017: Effects of the relaxation of upwelling-favorable winds on the diurnal and semidiurnal water temperature fluctuations in the Santa Barbara Channel California. *J. Geophys. Res. Oceans*, doi:10.1002/2017JC013199, in press.

Bane, J. M., M. D. Levine, R. M. Samelson, S. Haines, M. Meaux, N. Perlin, P. M. Kosro, and T. Boyd, 2005: Atmospheric forcing of the Oregon coastal ocean during the 2001 upwelling season. *J. Geophys. Res.*, **110**, C10S02, doi:10.1029/2004JC002653.

Battisti, D. S., and B. M. Hickey, 1984: Application of remote wind-forced coastal trapped wave theory to the Oregon and Washington coasts. *J. Phys. Oceanogr.*, **14**, 887–903, doi:10.1175/1520-0485(1984)014<0887:AORWFC>2.0.CO;2.

Björnsson, H., and S. A. Venegas, 1997: A manual for EOF and SVD analyses of climate data. Centre for Climate and Global Change Research Rep. 97-1, McGill University, 52 pp.

Bond, N. A., C. F. Mass, and J. E. Overland, 1996: Coastally trapped wind reversals along the United States west coast during the warm season. Part I: Climatology and temporal evolution. *Mon. Wea. Rev.*, **124**, 430–445, doi:10.1175/1520-0493(1996)124<0430:CTWRAT>2.0.CO;2.

Brink, K. H., 1991: Coastal-trapped waves and wind-driven currents over the continental shelf. *Annu. Rev. Fluid Mech.*, **23**, 389–412, doi:10.1146/annurev.fl.23.010191.002133.

Castelao, R. M., and Y. Wang, 2014: Wind-driven variability in sea surface temperature front distribution in the California Current System. *J. Geophys. Res. Oceans*, **119**, 1861–1875, doi:10.1002/2013JC009531.

Chan, F., J. A. Barth, J. Lubchenco, A. Kirincich, H. Weeks, W. T. Peterson, and B. A. Menge, 2008: Emergence of anoxia in the California Current large marine ecosystem. *Science*, **319**, 920, doi:10.1126/science.1149016.

Connolly, T. P., B. M. Hickey, S. L. Geier, and W. P. Cochlan, 2010: Processes influencing seasonal hypoxia in the northern California Current System. *J. Geophys. Res.*, **115**, C03021, doi:10.1029/2009JC005283.

Edwards, K. A., D. P. Rogers, and C. E. Dorman, 2002: Adjustment of the marine atmospheric boundary layer to the large-scale bend in the California coast. *J. Geophys. Res.*, **107**, 3213, doi:10.1029/2001JC000807.

Evans, W., B. Hales, P. Strutton, K. Shearman, and J. Barth, 2015: Failure to bloom: Intense upwelling results in negligible phytoplankton response and prolonged CO_2 outgassing over the Oregon shelf. *J. Geophys. Res. Oceans*, **120**, 1446–1461, doi:10.1002/2014JC010580.

Fawcett, A., G. Pitcher, and F. Shillington, 2008: Nearshore currents on the southern Namaqua shelf of the Benguela upwelling system. *Cont. Shelf Res.*, **28**, 1026–1039, doi:10.1016/j.csr.2008.02.005.

Fewings, M. R., L. Washburn, and J. C. Ohlmann, 2015: Coastal water circulation patterns around the Northern Channel Islands and Point Conception, California. *Prog. Oceanogr.*, **138A**, 283–304, doi:10.1016/j.pocean.2015.10.001.

——, ——, C. E. Dorman, C. Gotschalk, and K. Lombardo, 2016: Synoptic forcing of wind relaxations at Pt. Conception, California. *J. Geophys. Res. Oceans*, **121**, 5711–5730, doi:10.1002/2016JC011699.

Flynn, K. R., M. R. Fewings, C. Gotschalk, and K. Lombardo, 2017: Large-scale anomalies in sea-surface temperature and air-sea fluxes during wind relaxation events off the United States West Coast in summer. *J. Geophys. Res. Oceans*, **122**, 2574–2594, doi:10.1002/2016JC012613.

Fore, A. G., B. W. Stiles, A. H. Chau, B. A. Williams, R. S. Dunbar, and E. Rodríguez, 2014: Point-wise wind retrieval and ambiguity removal improvements for the QuikSCAT climatological data set. *IEEE Trans. Geosci. Remote Sens.*, **52**, 51–59, doi:10.1109/TGRS.2012.2235843.

García-Lafuente, J., J. Delgado, F. Criado-Aldeanueva, M. Bruno, J. del Río, and J. M. Vargas, 2006: Water mass circulation on the continental shelf of the Gulf of Cádiz. *Deep-Sea Res. II*, **53**, 1182–1197, doi:10.1016/j.dsr2.2006.04.011.

Garel, E., I. Laiz, T. Drago, and P. Relvas, 2016: Characterisation of coastal counter-currents on the inner shelf of the Gulf of Cadiz. *J. Mar. Syst.*, **155**, 19–34, doi:10.1016/j.jmarsys.2015.11.001.

Garreaud, R. D., J. A. Rutllant, and H. Fuenzalida, 2002: Coastal lows along the subtropical west coast of South America: Mean structure and evolution. *Mon. Wea. Rev.*, **130**, 75–88, doi:10.1175/1520-0493(2002)130<0075:CLATSW>2.0.CO;2.

Grantham, B., F. Chan, K. Nielsen, D. Fox, J. Barth, A. Huyer, J. Lubchenco, and B. Menge, 2004: Upwelling-driven nearshore hypoxia signals ecosystem and oceanographic changes in the northeast Pacific. *Nature*, **429**, 749–754, doi:10.1038/nature02605.

Hales, B., J. N. Moum, P. Covert, and A. Perlin, 2005a: Irreversible nitrate fluxes due to turbulent mixing in a coastal upwelling system. *J. Geophys. Res.*, **110**, C10S11, doi:10.1029/2004JC002685.

——, T. Takahashi, and L. Bandstra, 2005b: Atmospheric CO_2 uptake by a coastal upwelling system. *Global Biogeochem. Cycles*, **19**, GB1009, doi:10.1029/2004GB002295.

——, L. Karp-Boss, A. Perlin, and P. A. Wheeler, 2006: Oxygen production and carbon sequestration in an upwelling coastal margin. *Global Biogeochem. Cycles*, **20**, GB3001, doi:10.1029/2005GB002517.

Halliwell, G. R., and J. S. Allen, 1987: The large-scale coastal wind field along the west coast of North America, 1981–1982. *J. Geophys. Res.*, **92**, 1861–1884, doi:10.1029/JC092iC02p01861.

Hannachi, A., I. T. Jolliffe, and D. B. Stephenson, 2007: Empirical orthogonal functions and related techniques in atmospheric science: A review. *Int. J. Climatol.*, **27**, 1119–1152, doi:10.1002/joc.1499.

Hickey, B. M., 1979: The California Current system—Hypotheses and facts. *Prog. Oceanogr.*, **8**, 191–279, doi:10.1016/0079-6611(79)90002-8.

Horel, J. D., 1984: Complex principal component analysis: Theory and examples. *J. Climate Appl. Meteor.*, **23**, 1660–1673, doi:10.1175/1520-0450(1984)023<1660:CPCATA>2.0.CO;2.

Huyer, A., 1983: Coastal upwelling in the California Current system. *Prog. Oceanogr.*, **12**, 259–284, doi:10.1016/0079-6611(83)90010-1.

Karp-Boss, L., P. A. Wheeler, B. Hales, and P. Covert, 2004: Distributions and variability of particulate organic matter in a coastal upwelling system. *J. Geophys. Res.*, **109**, C09010, doi:10.1029/2003JC002184.

Kelly, K. A., 1985: The influence of winds and topography on the sea surface temperature patterns over the northern California slope. *J. Geophys. Res.*, **90**, 11 783–11 798, doi:10.1029/JC090iC06p11783.

Mass, C. F., and N. A. Bond, 1996: Coastally trapped wind reversals along the United States west coast during the warm season. Part II: Synoptic evolution. *Mon. Wea. Rev.*, **124**, 446–461, doi:10.1175/1520-0493(1996)124<0446:CTWRAT>2.0.CO;2.

Melton, C., L. Washburn, and C. Gotschalk, 2009: Wind relaxations and poleward flow events in a coastal upwelling system on the central California coast. *J. Geophys. Res.*, **114**, C11016, doi:10.1029/2009JC005397.

Merrifield, M., and R. Guza, 1990: Detecting propagating signals with complex empirical orthogonal functions: A cautionary note. *J. Phys. Oceanogr.*, **20**, 1628–1633, doi:10.1175/1520-0485(1990)020<1628:DPSWCE>2.0.CO;2.

Nelson, C. S., 1977: Wind stress and wind stress curl over the California Current. NOAA Tech. Rep. NMFS SSRF-714 (NTIS PB-273610), 87 pp., https://swfsc.noaa.gov/publications/CR/1977/7737.PDF.

North, G. R., T. L. Bell, R. F. Cahalan, and F. J. Moeng, 1982: Sampling errors in the estimation of empirical orthogonal functions. *Mon. Wea. Rev.*, **110**, 699–706, doi:10.1175/1520-0493(1982)110<0699:SEITEO>2.0.CO;2.

Nuss, W. A., 2007: Synoptic-scale structure and the character of coastally trapped wind reversals. *Mon. Wea. Rev.*, **135**, 60–81, doi:10.1175/MWR3267.1.

——, and Coauthors, 2000: Coastally trapped wind reversals: Progress toward understanding. *Bull. Amer. Meteor. Soc.*, **81**, 719–743, doi:10.1175/1520-0477(2000)081<0719:CTWRPT>2.3.CO;2.

Pauly, D., and V. Christensen, 1995: Primary production required to sustain global fisheries. *Nature*, **374**, 255–257, doi:10.1038/374255a0.

Perlin, N., R. M. Samelson, and D. B. Chelton, 2004: Scatterometer and model wind and wind stress in the Oregon-northern California coastal zone. *Mon. Wea. Rev.*, **132**, 2110–2129, doi:10.1175/1520-0493(2004)132<2110:SAMWAW>2.0.CO;2.

Relvas, P., and E. D. Barton, 2002: Mesoscale patterns in the Cape São Vicente (Iberian Peninsula) upwelling region. *J. Geophys. Res.*, **107**, 3164, doi:10.1029/2000JC000456.

——, and ——, 2005: A separated jet and coastal counterflow during upwelling relaxation off Cape Sao Vicente (Iberian Peninsula). *Cont. Shelf Res.*, **25**, 29–49, doi:10.1016/j.csr.2004.09.006.

Renault, L., C. Deutsch, J. C. McWilliams, H. Frenzel, J.-H. Liang, and F. Colas, 2016: Partial decoupling of primary productivity from upwelling in the California Current system. *Nat. Geosci.*, **9**, 505–508, doi:10.1038/ngeo2722.

Rogerson, A., 1999: Transcritical flows in the coastal marine atmospheric boundary layer. *J. Atmos. Sci.*, **56**, 2761–2779, doi:10.1175/1520-0469(1999)056<2761:TFITCM>2.0.CO;2.

Samelson, R., and Coauthors, 2002: Wind stress forcing of the Oregon coastal ocean during the 1999 upwelling season. *J. Geophys. Res.*, **107**, 3034, doi:10.1029/2001JC000900.

SeaPAC, 2016: QuikSCAT Level 2B ocean wind vectors in 12.5-km slice composites version 3.1. PO.DAAC, accessed 7 September 2017, doi:10.5067/QSX12-L2B31.

Send, U., R. C. Beardsley, and C. D. Winant, 1987: Relaxation from upwelling in the Coastal Ocean Dynamics Experiment. *J. Geophys. Res.*, **92**, 1683–1698, doi:10.1029/JC092iC02p01683.

Siedlecki, S. A., N. S. Banas, K. A. Davis, S. Giddings, B. M. Hickey, P. MacCready, T. Connolly, and S. Geier, 2015: Seasonal and interannual oxygen variability on the Washington and Oregon continental shelves. *J. Geophys. Res. Oceans*, **120**, 608–633, doi:10.1002/2014JC010254.

Taylor, S. V., D. R. Cayan, N. E. Graham, and K. P. Georgakakos, 2008: Northerly surface winds over the eastern North Pacific Ocean in spring and summer. *J. Geophys. Res.*, **113**, D02110, doi:10.1029/2006JD008053.

Thomson, R. E., and W. J. Emery, 2014: *Data Analysis Methods in Physical Oceanography.* 3rd ed. Elsevier, 654 pp.

Wallace, J. M., and R. E. Dickinson, 1972: Empirical orthogonal representation of time series in the frequency domain. Part I: Theoretical considerations. *J. Appl. Meteor.*, **11**, 887–892, doi:10.1175/1520-0450(1972)011<0887:EOROTS>2.0.CO;2.

Washburn, L., M. Fewings, C. Melton, and C. Gotschalk, 2011: The propagating response of coastal circulation due to wind relaxations along the central California coast. *J. Geophys. Res.*, **116**, C12028, doi:10.1029/2011JC007502.

Winant, C., R. Beardsley, and R. Davis, 1987: Moored wind, temperature, and current observations made during Coastal Ocean Dynamics Experiments 1 and 2 over the northern California continental shelf and upper slope. *J. Geophys. Res.*, **92**, 1569–1604, doi:10.1029/JC092iC02p01569.